Investigating the Andromeda Stream: A Simple Analytic Bulge-Disk-Halo Model for M31

by
Jonathan James Geehan
B.Sc. (Honours), Memorial University of Newfoundland, 2002

A Thesis Submitted in Partial Fulfillment of the
Requirements for the Degree of

MASTER OF SCIENCE

in the Department of Physics and Astronomy

Supervisor: Dr. A. Babul

Abstract

The work presented in this thesis is the first step in a larger study of M31's giant southern stream and its origins. We construct simple analytic models for the potential of the M31 galaxy to provide an easy basis for calculating orbits in M31's halo. We use an NFW dark halo, an exponential disk, a Hernquist bulge, and a central point mass to describe the gravitational potential of the galaxy. We constrain the parameters of these functions by comparing to existing surface brightness, velocity dispersion, and rotation curve measurements of M31. Our description provides a good fit to the observations and agrees well with more sophisticated modelling of M31. While in many respects the parameter set is well constrained, there is substantial uncertainty in the outer halo potential and a near-degeneracy between the disk and halo components, producing a large, nearly 2-dimensional allowed region in parameter space. We limit this allowed region using theoretical expectations for the halo concentration, baryonic content, mass within 125 kpc, and stellar M/L ratio, finding a smaller region where the parameters are physically plausible yet still providing a good fit to the observations. We compare test-particle orbits in our galaxy potential to those produced with simpler analytic models that have been used recently for models of the stellar stream.

Table of Contents

List of Tables

List of Figures

Acknowledgments

Wow! It's been two and half years since I started my masters program at the University of Victoria. So much has happened in that amount of time and I've met so many people, it would be impossible to describe how much each one has helped me in my years here in Victoria.

First off, I must thank the people who helped me so much during the course of this work. I'd like to thank my supervisor Arif Babul for his help, guidance and financial support over the last few years. Also Raja Guhathakurta for his helpful discussions in person and via e-mail. Larry Widrow for answering questions and making suggestions, and for providing me with much of the data used in this work. I can't forget Mark Fardal, who was such a huge help in this work. I can't thank him enough for taking the time to answer all those silly questions I had when it seemed like he had a million other things to do at the time. Without his help I don't think this project would have turned out as well as it has.

Secondly, I'd like to thank all the staff and other faculty who gave some of their time to answer my questions and give me advice along the way. There are too many to name here, but if you're reading these acknowledgments then you would know who you are. I really appreciated it.

Thirdly, those crazy fellow grad students of mine. We've had so many fun times (and some not so fun ones) that have made all the hard work seem not so hard. Also for all the help they've given me along the way, answering questions and showing me the tricks of the trade. Since I'm on the topic of grad students I can't forget my officemates: Jeff, Rachel, and Aaron. You three have made going into The Office a fun experience. You helped me through assignments and took my mind off work when I felt like it was going down the tubes. It was greatly appreciated!

Fourthly, I want to thank my girlfriend Stephanie and her family for all their

help and support over the last year and a half since I met her. Never had I imagined meeting such a wonderful woman on the other side of the country. Her love and support have helped me work through the difficult times in this work. I don't think I could have made it through without her.

Finally, I want to thank my family: my Mom, my aunt, and by brother. From the time when I was so young watching all those episodes of Star Trek and dreaming of becoming an astronomer they have always given me their love and support even though they were never understood what I was doing in school. Despite living on the other side of the country they were always only a phone call away, night or day, and always ready to listen to what was on my mind. It really helped me through, especially in my first year here when I was trying to get settled.

Thanks everyone, for everything.

Chapter 1

Introduction

The hierarchical galaxy formation scenario states that galaxies form by the merging of smaller bodies. The scenario predicts that the halo of a galaxy should exhibit evidence for ancient and recent mergers in the form of substructure. As a larger galaxy consumes a smaller satellite galaxy, tidal forces due to the larger galaxy unbind stars from the satellite galaxy resulting in leading and trailing stellar streams. It is possible for these streams to remain coherent for several billion years (Johnston et al., 1996; Helmi and White, 1999). This amount of time provides an opportunity to study these stellar streams in the halos of large galaxies and consequently test the hierarchical clustering paradigm. Not only can we test this scenario, but we can also learn important details about galaxy formation, such as the frequency of merger events and the properties of the components of the merger.

Unfortunately it is not an easy task to identify and quantify substructure in the halos of large galaxies. It is hindered by the fact that to study a stream, one must resolve and measure the individual stars in the halo. This is a challenging task and at present is only possible with galaxies in our local group. Detailed studies of the halo of our own galaxy have proven fruitful. Coherent structures, such as stellar streams are identified using star counts, distance measurements (if available,) and velocity

correlations. Such features have been discovered in the halo of the Milky Way galaxy (see Ferguson et al., 2002, for a summary). One such feature is the discovery of the tidal disruption of the Sagittarius dwarf galaxy and its associated stellar stream (eg., Ibata et al., 1995; Mateo et al., 1998; Majewski et al., 1999; Yanny et al., 2000; Ibata et al., 2001b,c). Another is the large ring of old stars that may encircle the Milky Way which may possibly be the remnants of an ancient merger (Ibata et al., 2003; Yanny et al., 2003), however the actual origin of this feature still remains a mystery. There is a problem with making observations of substructure in our own galaxy as noted by Newberg et al. (2002) due to our location in one of the spiral arms of the Milky Way. These authors in their survey of the Milky Way's halo found contamination from interstellar dust cloud in their star count map, which makes it difficult to identify what is halo substructure and what is not. Also, in the case of the ring of stars encircling the Milky Way, to discover the extent of the ring one must look through the bright central regions of the galaxy which makes it difficult to count stars on the other side. This greatly complicates the study and understanding of these features. Our vantage point of M31 is not obscured by dust found in the plane of the Milky Way. For this reason the recent discovery of a giant stellar stream emanating from the southern part of the disk of the Andromeda galaxy is extremely interesting.

The giant southern stream was first reported by Ibata et al. (2001a). It was discovered through counts of red giant stars in the halo of M31, and since its discovery it has been a source of intense study using careful photometric and spectroscopic analysis. After its initial discovery follow-up studies extended the initial survey to outline the extent of the stream (Ferguson et al., 2002; McConnachie et al., 2003; Ferguson et al., 2004). These surveys discovered that the stream itself is well defined and extends away from us below the disk of M31, out to a distance of $\sim$ 100 kpc. Accurate distances at various locations along the length of the stream were determined from the magnitude of the tip of the RGB of the stream's population (McConnachie et al., 2003). These data were collected using the wide-field CCD camera at the

Canada-France-Hawaii Telescope surveying the M31 stream, resolving stars down the red giant branch down to I≃25. The tip of the RGB is an effective way of measuring astronomical distances since tip of the RGB is relatively insensitive to variations in metallicity in the I-band. To use this method to measure distance one must determine the I-band distance modulus, which requires knowledge of the I-band apparent (I) and absolute (M_I) magnitude of the tip. Originally the estimate of the apparent magnitude of the tip was done using eye estimates, however a method to formally define the tip was developed by Lee et al. (1993). The tip is identified by the sharp cutoff it produces in the I-band RGB luminosity function. This cutoff can be detected using an edge detecting algorithm, in this case the Sobel filter. The absolute magnitude of the tip can be estimated from the bolometric magnitude (M_{bol}) and the I-band bolometric correction (BC_I). Using relationships between the metallicity and M_{bol} and the (V−I) colour and BC_I provided in Lee et al. (1993) one can estimate the absolute magnitude of the tip of the RGB and hence the distance. Spectroscopy done by Ibata et al. (2004); Guhathakurta et al. (2005) has provided absorption-line estimates of the metallicity along the stream, and revealed that the stream has a strong velocity gradient along its body with the outer regions being almost at rest with respect to M31 while the inner regions are approaching us at 300 km s^{-1} with respect to M31. Guhathakurta et al. (2005) collected their data using the Deep Imaging Multi-Object Spectrograph (DEIMOS) on the Keck 10 m telescope and made a photometric estimate of the metallicity of the RGB stars by fitting RGB fiducials in the colour-magnitude diagram. They also made a spectroscopic estimate of the metallicity using the CaII triplet strength and an empirical calibration relation based on luminous RGB stars in the Milky Way. Ibata et al. (2004) also used the DEIMOS spectrograph on the Keck telescope to make their spectrographic survey of M31's stream and halo. The radial velocities of the stars in their survey were measured with respect to standard stars observed during the observing run. This velocity gradient suggests that the stream is similar to the extended tidal tails of the Sagittarius dwarf

galaxy that wrap around the Milky Way (Totten and Irwin, 1998).

Despite all the observational effort that has been put into these studies we still do not know whether the progenitor of the stream has survived the merger process, and if so, where it is. There are many faint features in the inner halo of M31 that have been suggested as possibilities. Fardal et al. (2005) briefly describes these possible candidates:

Linear Continuation: McConnachie et al. (2003) observed two fields along the linear projection of the southern stream on the other side of the disk. Both Ibata et al. (2004) and Font et al. (2005) found it difficult to fit this feature in their orbital fits, so it is questionable whether this feature is actually associated with the stream, however it is possible that the stream scatters enough debris upon pericentre passage to this side to produce the stars seen in these fields.

NGC 205: NGC 205 is close to the projection of the stream on the other side of M31. This suggests that it may be associated with the stream, however its velocity has the opposite sign from that of the stream. In addition, the bluer colour of the red giants indicate a lower metallicity when compared to the stream, arguing against a connection between the two.

NGC 205 Loop: Discussed in Ferguson et al. (2005) this small loop of stars ($\sim$ 15 kpc) appears to emanate from NGC 205, at least in projection. This geometry suggests a possible connection between the two. The analysis of this feature's CMB by Ferguson et al. (2005) showed that it was similar to the giant southern stream and NE Shelf (see below) in that it has an extended blue horizontal branch.

M32: M31's other prominent nearby satellite galaxy is an obvious candidate for the origin of the stream given that it lies almost directly on the path of the stream. In fact, it was proposed as a candidate for the progenitor of the stream when it was first discovered (Ibata et al., 2001a). However, as with NGC 205, its radial

velocity has the wrong sign for it to lie within the southern stream. Due to its complex metallicity distribution it is unclear whether or not it is consistent with the stream.

Merrett et al. Planetary Nebulae: A number of planetary nebulae in the disk of M31 were found to have velocities that were inconsistent with the kinematics of the disk in the survey by Merrett et al. (2003). Most move in a direction opposite to the local disk rotation, though some move in the same direction but with larger speeds. A subset of these on the northeast side occupy a narrow region in position-velocity space (Merrett et al., 2004). Merrett et al. fit an orbit connecting this group to the stream using their simpler potential, but did not demonstrate agreement with the detailed properties of the stream.

Northern Spur: A faint clump of stars to the NE end of M31 were shown in the star-count maps of Ferguson et al. (2002). This feature is referred to as the Northern Spur. The RGB colour of this feature is similar to that of the stream (Ferguson et al., 2002) and is a prominent candidate for the continuation of the stream (Merrett et al., 2003). Further analysis done by Ferguson et al. (2005) indicates that this feature contains an old stellar population. Its CMD also indicates that it contains an asymptotic giant branch (AGB) population. Radial velocity measurements of the Spur region show that its velocity is different from that of the disk in this region suggesting that it is a distinct object (Ferguson et al., 2004). Merrett et al. (2004) found an overdensity of planetary nebulae in this region with a wide range of velocities. Some were consistent with the disk velocity, some had larger velocities, while some had the wrong sign altogether. These authors inferred that the Spur represents a warp in the disk of M31. If the progenitor does lie in the Northern Spur region, its velocity cannot be reliably constrained at present due to possible contamination from the disk and presence of opposing velocities (Fardal et al., 2005).

NE Shelf: Ferguson et al. (2005) describe this feature found in M31's halo to the north-east of the galaxy's centre as a large overdensity of stars which has a sharp outer boundary. Their analysis of the CMD of this feature revealed some similarities to the CMD of the southern stream. Both CMDs showed RGB bumps at I=$\sim$ 25.1. This is due to an evolutionary pause during the RGB phase of a stars life when the H-burning shell passes through the deepest penetration of the convective core. They also inferred from the RGB colour that both this feature and the giant southern stream contain relatively metal-rich stellar populations. Ferguson et al. (2005) also analyzed the luminosity functions of both this feature and the stream and suggest that the differences between the two populations are small. They further suggest that the differences between the red clumps in the two CMDs is due to different line-of-sight distances for the two features.

And NE: This is a low surface brightness enhancement far out along the major axis of M31 and was discussed by Zucker et al. (2004). There is no visible connection between this feature and the stream, and the luminosity is probably too low for it to be an intact progenitor.

MrED: Discussed by Ferguson et al. (2002), this diffuse surface brightness enhancement on the eastern side of M31 contains high-metallicity red giants, given their colour. Fardal et al. (2005) refer to this as the metal-rich eastern diffuse (MrED) feature. Font et al. (2005) find an orbit that matches this feature, however the low surface brightness of this feature argues against it being the progenitor. It might represent debris from the continuation of the stream, however this is still not clear.

And VIII: This feature is a group of objects with abnormal radial velocities in the M31 disk (Morrison et al., 2003) made up of planetary nebulae, globular clusters,

and HI detections. This feature lies nearly across the stream and has a velocity consistent with it. It does have one feature which is not expected for a progenitor moving along the stream: it is extended for $\sim 1^\circ$ transverse to the stream. If this is the progenitor then is has probably already passed through pericentre.

G1 Clump: This is a diffuse surface brightness enhancement identified by Ferguson et al. (2002) in the vicinity of the globular cluster G1. Ferguson et al. (2005) found that the colour-magnitude diagram for this feature showed evidence for a young stellar population, exhibiting a well-populated upper main sequence. Further the colour-magnitude diagram of the clump differs from that of the southern stream, suggesting that the two may not be associated.

One way to identify and discover the fate of the progenitor is to construct a fairly accurate and realistic description of the gravitational potential of M31, and use that potential to calculate orbits for the stream using the properties of the stream to constrain the orbit. Some progress has already been made on this front by Ibata et al. (2004) and Font et al. (2005). Ibata et al. (2004) tested several simple toy potentials and a more sophisticated bulge-disk-halo model, however only provided model parameters for their toy potentials. Font et al. (2005) computed orbits in a simple analytic bulge-disk-halo potential (not optimized to match M31). They found rough agreement for their potential and the stream, however, their orbits were not optimized, instead their work focused more on the physical implications of the width and velocity dispersion of the stream. A detailed study of the stream dynamics and of its progenitor orbit requires a realistic mass model that is in accord with observations of M31 and numerical results for dark matter halos. It is also desirable that the potential be simple and easy to use for the purposes of orbit calculations, and easily adaptable for more detailed future numerical and semi-analytic analysis.

There have been many efforts to model the mass distribution of M31. The first efforts were made by Babcock (1938), Babcock (1939), Wyse and Mayall (1942),

Schwarzschild (1954), and Schmidt (1957). Improvements in the quality of photometric and spectroscopic data in the 70's and 80's led to improvements on these existing models by Deharveng and Pellet (1975), Monnet and Simien (1977), Simien et al. (1979), and Kent (1989). Since in recent years we have gained new understanding of the shape and nature of the dark halos surrounding these large spiral galaxies these models must be updated again. The most recent efforts made to improve these models have been made by Klypin et al. (2002), and Widrow et al. (2003). These two groups developed sophisticated mass models, however, they are neither simple nor easy to use, especially for the purposes of orbit calculations. The mass models of Widrow et al. (2003) are specified in terms of a set of distribution functions and while they can be used to compute the mass density distribution and the associated gravitational potential, the derivation is implicit and must be done iteratively. In other words a closed analytic form that describes the density and potential that accurately describes the dark halo of M31 is not available. Similarly, the mass model of Klypin et al. (2002) also does not exist in a closed analytic form.

The work presented in this thesis will further improve on the previous work done on modelling M31 by presenting a simple, yet reasonably accurate analytic description of the mass distribution and potential of the galaxy. The main goal of this work is to provide a description of M31's potential that is suitable for the purposes of calculating satellite orbits. The first step in this work is to decompose M31 into four components: the central black hole (BH), the bulge, the disk, and the extended dark halo. The mass of these components are modelled using simple well-known functional forms whose associated potentials are easy to compute. The structural parameters describing these components are determined by requiring the model to be in agreement with M31's observed surface brightness profile, disk rotation curve, bulge velocity dispersion profile, and total mass distribution. In Chapter 2 of this thesis, we will discuss the functional forms we have chosen for our four component model and their associated structural parameters. In Chapter 3 we review the M31 observations

used to constrain the parameters of our model, and visually compare them to our best-fit model. In Chapter 4 we discuss some general features of our best-fit solution and whether our best-fit model is physically reasonable. Due to problems with the physical reality of our model we introduce further constraints on our model resulting in what we call our "constrained best-fit" model. We also compare our potential to other recently published simple analytic potentials for M31. In Chapter 5 we first review the observations of the stream that we use as constraints on our orbit. We then compute sample test particle orbits, using our "constrained best-fit" model, for the progenitor of the giant southern stream to illustrate the effects that the amplitude and the geometry of the potential have on the orbits. We also compare our orbits to other recently published orbits in some simple analytic potentials. A summary of the conclusions drawn from this work are presented in Chapter 6.

Chapter 2

Components of the M31 Mass Model

As mentioned previously the mass model developed through the course of this work is a four component, black hole-bulge-disk-halo model. In reality the innermost regions of M31 are more complicated, and a model which is concerned with modelling these regions properly ought to include not only a central black hole and bulge, but also a nucleus, a bar, and a spheroid. The disk in our model is a single component, however in reality it is also a more complicated component and a more detailed model of this region of the galaxy should include a thick and thin stellar disk, and a thin gaseous disk. However our purpose in this work is to develop a model which is as simplistic as possible and yet match the available observational data on M31, so in the interests of keeping our model simple we restrict ourselves to only four components, the central black hole, the bulge, the disk, and the extended dark halo. Also in keeping with our goal we use simple analytic functions to describe these four components. To use these simple functions to describe these components several simplifying assumptions must be made. These assumptions and our choice of functional forms are discussed below. For completeness we use a spatially flat ΛCDM

cosmology with a Hubble constant of $H = 100h$ km s^{-1} Mpc^{-1}, with h chosen to be 0.71. The density of matter in a spatially flat universe is defined to be $\Omega_m = \rho/\rho_c$, where $\rho_c = 3h^2/8\pi G = 277.72h^2$ M$_\odot$ kpc^{-3} is the critical density which determines if the universe is closed or open, and ρ is the density of the universe. If $\rho > \rho_c$ then the universe will eventually collapse, and if $\rho < \rho_c$ then the universe will continue to expand. Here we have chosen $\Omega_m = 0.14h^{-2}$ and $\Omega_b = 0.024h^{-2}$ where Ω_b is the density of baryons in the universe (Spergel et al., 2003). Note that all values are present-day epoch. We also use the spherical approximation, $v_c^2 = GM/r^2$ to relate the rotational velocity and the mass of M31, where r is the distance from the centre of M31.

2.1 The Central Black Hole

As briefly discussed above, the central region of M31 is presumed to comprise of not only a central black hole, but also a small-scale stellar nuclear component that is photometrically and dynamically distinct from the bulge and the large-scale galactic disk (see Kormendy and Richstone, 1995, and references therein). Estimates of the mass of the central black hole range from (3-8.5)$\times 10^7$ M$_\odot$ (Dressler and Richstone, 1988; Bacon et al., 2001) while mass estimates of the nuclear component range from (1.5-2)$\times 10^7$ M$_\odot$ within $\sim$ 10 pc (Bacon et al., 2001; Peng, 2002; Salow and Statler, 2004).

Again in keeping with the spirit of this work we adopted the most simple model for the central black hole, a point mass located at the centre of our system. We also fixed the mass of the black hole to the recently derived mass of $M_{BH} = (5.6 \pm 0.7) \times 10^7$ M$_\odot$ made by Salow and Statler (2004). This mass is also in excellent agreement with black hole mass estimates made by Tremaine et al. (2002) of $M_{BH} = (5.5 \pm 1.5) \times 10^7$ M$_\odot$ from the M_{BH}-σ correlation. The presence of the central black hole as part of the potential of M31 only becomes important for scales $r < 20$ pc. Due to the fact that

the mass contained in the nuclear component is less than half the mass of the black hole we chose to ignore this component. We initially added a black hole to our model to test its effect on the bulge velocity dispersions and have since kept it only for completeness.

2.2 The Galactic Bulge

We modelled the bulge component of M31 as a spherically symmetric mass distribution represented by a Hernquist profile (Hernquist, 1990)

$$\rho_B(r) = \left(\frac{M_B}{2\pi r_B^3}\right)\frac{1}{(r/r_B)(1+r/r_B)^3}, \tag{2.1}$$

where M_B is the total mass of the bulge and r_B is its scale radius. These two parameters will be determined using observational constraints. The corresponding mass profile and potential for this density distribution are

$$M_B(r) = \frac{M_B r^2}{(r_B+r)^2}, \tag{2.2}$$

$$\Phi_B(r) = -\frac{GM_B}{r_B+r}. \tag{2.3}$$

It is worth noting at this point that we also considered using the more general density profile of Dehnen (1993) where $\rho_B(r) \propto (r/r_B)^{-\gamma}(1+r/r_B)^{\gamma-3}$ which was developed because the luminosity profile of de Vaucouleurs (1948) cannot be deprojected into the spatial density or the gravitational potential analytically and therefore was difficult to use in detailed modelling of galaxies. The density for these profiles is proportional to r^{-4} at large radii and diverges as $r^{-\gamma}$ in the centre. We found that for the range of $0.1 \leq \gamma \leq 2$ the results were all equally good, in terms of the optimizing process we outline in this thesis. Therefore we opted to use the $\gamma = 1$ Hernquist profile. We found that both the bulge mass and the bulge mass-to-light ratio were quite

insensitive to variations in γ within the range noted above. This insensitivity to the precise nature of the inner density profile of the bulge used gives us confidence that the bulge parameters quoted in Tables 3 and 4.2, and generally that our bulge-disk decomposition, are robust.

It is well known that the bulge of M31 itself is not spherical. Detailed modelling based on surface photometry suggests that the bulge ought to be modelled as an oblate spheroid with an axis ratio of ~ 0.8 (Kent, 1983, 1989; Peng, 2002; Widrow et al., 2003) and that it is almost certainly triaxial (Lindblad, 1956; Stark, 1977; Kent, 1989; Stark and Binney, 1994). In avoiding the use of a more complicated non-spherical mass distribution, our decision to use a spherically symmetric distribution is guided by the fact that our primary purpose is to construct orbits to model the giant southern stream. The stream itself has an estimated pericentre of 1.8 to 6.5 kpc, and an apocentre of $\sim$ 100 kpc (Ibata et al., 2004; Font et al., 2005), therefore the progenitor spends little to no time in a region where the asphericity of the bulge could have any dynamical effect. It is also worth noting that the equipotential surfaces tend to be more spherical than the mass distribution. However, if one uses our models for treatments of the dynamics at smaller radii, this spherical simplification should be kept in mind.

2.3 The Galactic Disk

In developing our model for the disk of M31 we assume, as suggested by the observations of Walterbos and Kennicutt (1987), that the mass distribution of the disk can be described by an exponential surface density profile:

$$\Sigma_D(R) = \Sigma_0 e^{-R/R_D}, \tag{2.4}$$

where Σ_0 is the central surface density, R_D is the scale length of the disk, and R is the distance from the centre of M31 in the plane of the disk. This corresponds to a

disk mass within a sphere of radius r of

$$M_D = 2\pi\Sigma_0 R_D^2\Big[1-(1+r/R_D)e^{-r/R_D}\Big]. \tag{2.5}$$

Here, $r = \sqrt{R^2+z^2}$ is the distance from the centre of M31 and z is the distance perpendicular to the plane of the disk.

In this work we consider two different representations of the disk. The first is an extremely simple toy model which we refer to as the "spherical disk" model. In this model we assume that the mass is distributed in a spherically symmetric fashion rather than in an axisymmetric disk. The corresponding gravitational potential resulting from this mass distribution is

$$\Phi_{D,sp}(r) = -2\pi G\Sigma_0 R_D^2\left[\frac{1-e^{-r/R_D}}{r}\right]. \tag{2.6}$$

Obviously this toy model is not a realistic representation of the disk of a spiral galaxy. The second model we consider is more realistic in that it represents the disk as an infinitesimally thin, axisymmetric mass distribution. The expression we used for the gravitational potential of this component was taken from Binney and Tremaine (1987) and it is given by:

$$\Phi_D(R,z) = -2\pi G\Sigma_0 R_D^2\int_0^\infty \frac{J_0(kR)e^{-k|z|}dk}{[1+(kR_D)^2]^{3/2}}, \tag{2.7}$$

where J_0 is a Bessel function of the first kind. We refer to this model as the "axisymmetric disk" model and unless stated otherwise the results presented in this thesis will be based on this model. The above expressions suggest that evaluating the potential and circular velocity profile for our axisymmetric model is more involved than for our spherical disk model. We found that for trivial orbit calculations where the test particle does not experience a strong gravitational force from the disk, the spherical model gives very similar results to the axisymmetric model with less computing time. Therefore our toy model is used to facilitate rapid orbit calculations for the

purposes of experimentation, as well as showing the effect that flattening the disk has on the derived orbits. The similarities and differences in the sample test particle orbits resulting from our two models will be discussed in Chapter 5.

2.4 The Extended Dark Halo

The final component of our model we discuss is the extended dark matter halo of M31. In keeping with the spirit of this work we model the dark halo as a spherically symmetric system. It is important to note that there is an issue concerning the sphericity of the halo, however it remains observationally unresolved, even in the case of the Milky Way. Therefore we adopt the simplest model for the halo. We adopt the NFW density profile of Navarro et al. (1996) to describe the run of density with radius:

$$\rho_H(r) = \frac{\delta_c \rho_c}{(r/r_H)(1 + r/r_H)^2}, \tag{2.8}$$

where ρ_c is the critical density quoted earlier, δ_c is a dimensionless density parameter, and r_H is the halo scale radius. N–body simulations based on the hierarchical clustering scenario within the cold dark matter cosmogony suggest that spherically averaged density profiles are well described by the above profile. There is still debate over the exact exponent of the density profile in the inner cusp, however this will not matter since the potential in the inner regions of our model will be dominated by the disk and/or bulge components.

The corresponding mass profile and potential for an NFW profile are given by the following expressions:

$$M_H(r) = 4\pi\delta_c\rho_c r_H^3 \left[\ln\frac{r + r_H}{r_H} - \frac{r}{r + r_H}\right], \tag{2.9}$$

$$\Phi_H(r) = -4\pi G\delta_c\rho_c r_H^2\left(\frac{r_H}{r}\right)\ln\left[\frac{r+r_H}{r_H}\right]. \tag{2.10}$$

Chapter 3

Specifying the M31 Model Parameters

The BH-bulge-disk-halo model described in the previous chapter has a total of seven structural parameters that remain to be specified: $M_{BH}, r_B, R_D, r_H, M_B, \Sigma_0$, and δ_c, however the black hole mass is fixed at the beginning leaving six parameters to be determined. In other words the parameters to be determined are a scale radius, and normalization for each of the bulge, disk, and halo components. We constrain these parameters using a number of available observations of M31.

Before discussing the details of the fitting process, we briefly review what is known about the configuration of M31. The galaxy itself lies at a distance of 784±24 kpc (Stanek and Garnavich, 1998) from the Milky Way, and has a mean radial velocity of -300 ± 4 km s^{-1} (de Vaucouleurs et al., 1991). The galaxy is oriented in the the sky slightly tilted with respect to edge on such that we look at it from below. This is evident from images of the disk dust lanes projected onto the bulge. For this work we assume an inclination of 77°, which is the generally accepted value, however, estimates range from 74° to 79° (Rubin and D'Odorico, 1969; Walterbos and Kennicutt, 1988; Ma et al., 1997). For reference an inclination of 90° corresponds to

an edge-on galaxy. The Andromeda galaxy spins counterclockwise on the sky. We assume a position angle for the disk of 37°. The position angle and inclination of M31 are illustrated in Figures 3.1 and 3.2. Note that the major axis of the bulge appears to be offset by $\sim+10°$ from the major axis of the disk and that the bulge isophotes are distinctly "box-shaped" in appearance with ellipticities that increase with radius. These two features of the bulge have generally been interpreted as indications of the triaxiality of the bulge (Lindblad, 1956; Stark, 1977; Kent, 1989; Stark and Binney, 1994). There is also evidence for a significant warp in the disk, especially in the outer regions, from analyses of HI and the light distribution of the disk (Sawa and Sofue, 1982; Innanen et al., 1982; Walterbos and Kennicutt, 1987; Morris et al., 1994).

There have been many detailed studies of M31 over the past two decades generating a large amount of kinematic and photometric data. In constraining our mass model we restrict ourselves to a limited number of data sets: specifically, the major axis and average surface brightness profiles, the bulge major and minor axis velocity dispersion, the disk rotation curve, and the mass estimates derived from dynamics in the inner and outer halo. These data sets are described in greater detail later in this chapter. To relate our mass model to the light profiles of the galaxy, we are required to introduce two additional parameters, the R-band mass-to-light ratios of the bulge, $(M/L_R)_B$, and the disk, $(M/L_R)_D$. In introducing these parameters we make the simplest possible assumption that these two ratios are constant over the entire bulge and disk. Given that there is only a modest colour gradient in M31 (Walterbos and Kennicutt, 1987) we feel this assumption is reasonably valid.

The introduction of these two mass-to-light ratios increases the number of parameters to be constrained to eight. In keeping with the main goal of this work to construct a simple mass model of M31 we need only get a close approximation to the surface brightness at all radii, which means not every feature will be followed. This is not such a large concern since some of the features are primarily features in the luminosity and not the mass. Note also that the abundance and quality of the

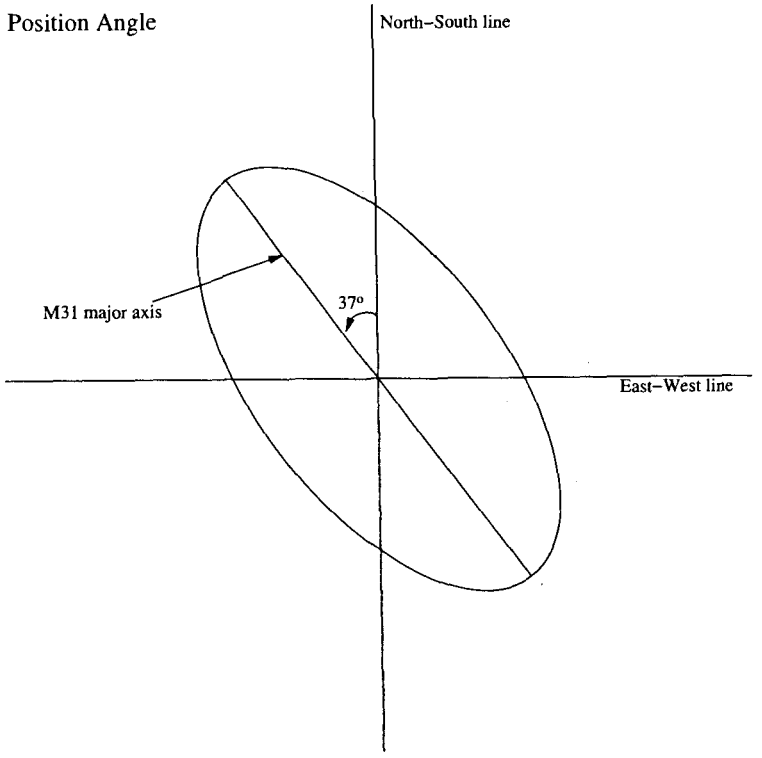

Figure 3.1 This figure shows the orientation of M31 in the sky. The position angle is the angle between the major axis of the disk and the north-south line with the angle increasing to the east.

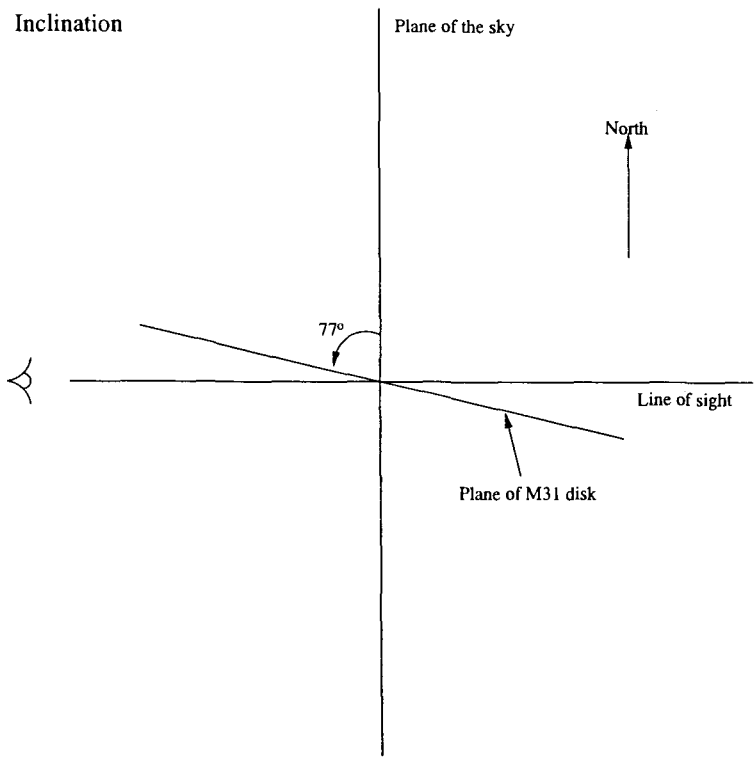

Figure 3.2 This figure shows the inclination of M31 in the sky. The inclination is measured from the plane of the sky to the plane of the disk with the angle increasing towards the observer.

surface brightness data is such that it would dominate the fit of the scale radii in any case. Keeping these points in mind the process of fitting these parameters was done in two steps. The first was to fit the two surface brightness profiles simultaneously to obtain the scale radii r_B and R_D of the bulge and the disk, and the luminosity normalization of these components. The χ^2 statistic from this fitting step is poor, which tells us that we did not fit all the higher-order details (i.e. bumps and wiggles) of the visual structure of M31, due, for example, to spiral arms, warps, dust lanes and other localized structures. However, overall the fit is quite good as we discuss later in § 3.1. Using the results from the surface brightness fit we then use the dynamical information to fit the four remaining parameters (the bulge and disk mass normalizations, M_B and Σ_0, and the two halo parameters, r_H and δ_c). Contrasting the χ^2 from the surface brightness fit, the χ^2 statistic from this fitting step is actually meaningful, since we are actually concerned with following the dynamical features of the bulge, disk, and halo since these tell about the distribution of mass. We later use this χ^2 statistic to constrain the allowed region of parameter space. Finally we combine the luminosity and mass normalizations for the bulge and disk to derive their respective mass-to-light ratios.

We determined the appropriate parameters for both the axisymmetric (flattened disk) and the toy spherical model. The parameters are summarized in Table 3. In the following sections we discuss in detail the observations used to constrain the models and how well our best-fit model compares. Discussion of errors, correlations, possible degeneracies between the parameters, and the correspondence between the allowed region of parameter space is left until Chapter 4.

3.1 M31 Surface Brightness Data

Given the fact that M31 is only $\sim$ 784 kpc from us, it has been the subject of detailed study since the 1930s, therefore there is quite a large amount of photometric

Table 3.1 M31 Mass Model Parameters for Best-fit Axisymmetric and Spherical Cases

Parameter	Symbol		Axisymmetric Model	Spherical Model
Black Hole Mass	M_{BH}	(10^7 $M_\odot$)	5.6	5.6
Total Bulge Mass	M_B	(10^{10} $M_\odot$)	2.8	2.7
Total Disk Mass	M_D	(10^{10} $M_\odot$)	11.8	14.2
Total Mass inside 125 kpc	$M(< 125$ kpc)	(10^{11} $M_\odot$)	6.1	7.3
Virial Mass	M^*_{200}	(10^{11} $M_\odot$)	7.2	9.0
	M^*_{100}	(10^{11} $M_\odot$)	7.9	9.9
Disk Mass within 1 scale radius	$M_D(< R_D)$	(10^{10} $M_\odot$)	3.1	3.7
Bulge Scale Radius	r_B	(kpc)	0.61	0.61
Disk Scale Radius	R_D	(kpc)	5.4	5.4
Halo Scale Radius	r_H	(kpc)	13.3	15.3
Virial Radius*	r_{200}	(kpc)	183.0	197.0
	r_{100}	(kpc)	236.0	255.0
Halo Density Parameter	δ_c	(10^4)	7.8	6.7
Halo Concentration Parameter	$C_{200} \equiv r_{200}/r_H$		13.7	12.8
Bulge M/L**	$(M/L_R)_B$		3.3	3.2
Disk M/L**	$(M/L_R)_D$		5.5	6.5
Disk Central Surface Density	Σ_0	(10^8 $M_\odot$/kpc^2)	6.5	7.7
Maximum Rotation Velocity	$V_{c,max}$	km/s	256.1	252.1
Fraction of "galactic" baryons	$\Omega_m(M_B + M_D)/(\Omega_b M_{200})$		1.2	1.1

* We define M_Δ as the mass enclosed with the sphere of radius R_Δ such that the mean density inside is $\Delta\rho_c$, where $\Delta = 100$ or 200 and $\rho_c = 277.72h^2$ $M_\odot$/kpc^2 is the present-day critical density.

** The quoted M/L ratios are based on luminosities that have *not* been corrected for internal or foreground extinction.

data available for this galaxy. To constrain the mass-to-light ratios and scale radii of our galaxy we use the azimuthally-averaged (or "global") and major axis surface brightness profiles. The advantage of using the global profile is that it minimizes effects from localized structural features, such as spiral arms, which can introduce bumps and wiggles in the light profile along any one direction. We would have preferred to use only the global light profile for these reasons, however most global profiles do not extend very far into the bulge, however major axis data does exist that probes into the regions where the bulge dominates the light. For this reason we also construct a major axis light profile using data from three different authors (Kent, 1983; Walterbos and Kennicutt, 1987; Lauer et al., 1993). We chose to use R-band data in our light profiles because we expect it to be less susceptible to effects from dust extinction and stellar population variations than bluer bands. Kent (1983) took two-colour images of the nucleus and bulge regions of M31 using an RCA CCD camera on the 61 cm telescope of the Whipple Observatory and on the Multiple-Mirror Telescope (MMT). Both of these telescopes are located on Mount Hopkins in Arizona. The data was obtained in the fall of 1981. He provided r-band surface brightness data for the inner $\sim 160''$ of the galaxy. Walterbos and Kennicutt (1987) obtained two-dimensional photographic photometry in various colours (U, B, V, and R). Their data was collected using the Burrell Schmidt telescope on Kitt Peak. They obtained major and minor axis light profiles along with a global light profile. Their major-axis light profile extends from $1'$ to $100'$ and their global light profile extends from $4'$ to $124'$. The final contributor to our major axis light profile is from Lauer et al. (1993) who used the HST Planetary Camera to obtain V- and I-band images of the inner regions of M31 (from $0.022''$ to $10.200''$). The Walterbos and Kennicutt data probe the outer regions of the profile, the Kent data the intermediate region, while the Lauer data probe the nuclear regions of the galaxy. The r-band and V-band data were converted to R-band using the following colours $r-R\approx0.35$ (Jorgensen, 1994) and $V-R\approx0.75$ (Tenjes et al., 1994). These colour transformations were also verified

Table 3.2 M31 Bulge Colours*.

Bulge Colour	Reference
r−R≈0.35	(Jorgensen, 1994)
B−r≈1.28	(Kent, 1987)
V−R≈0.75	(Tenjes et al., 1994)
B−R≈1.7	(Walterbos and Kennicutt, 1987)
B−V≈0.97	(Walterbos and Kennicutt, 1987; Tenjes et al., 1994)
V−K≈3.38	(Pritchet, 1977)
V−I≈1.34	(Lauer et al., 1993)
g−r≈0.55	(Hoessel and Melnick, 1980)
v−g≈0.78	(Hoessel and Melnick, 1980)

* All colours have an uncertainty of ±0.1

by running a stellar burst model in the PEGASE.2 population synthesis code (Fioc and Rocca-Volmerange, 1997) by one of the collaborators in this work, Mark Fardal. We found that for a 12 Gyr burst time there was agreement with ±0.1 mag arcsec^{-2} between our adopted V, r, and R offsets, as well as other measured colours of M31 presented in Table 3.2. In constructing our major axis profile we found it necessary to shift the Walterbos and Kennicutt (1987) data by −0.1 mag arcsec^{-2} to bring it in line with the other two data sets. Given an uncertainty of 0.1 in the colours as well as $\sim$ 0.1 mag arcsec^{-2} errors in the surface brightness measures, this level of fine-tuning to bring the data sets into line is not surprising. Since the global light profile is also derived from these same plates, we applied the same −0.1 mag arcsec^{-2} shift to this data as well. The mean surface brightness at radial coordinate r was computed by Walterbos and Kennicutt (1987) by averaging the light in elliptical annuli. These annuli were formed by taking a face-on circular ring of radius r and thickness δr, rotating it to an inclination of 77°, projecting this structure onto the plane of the sky, and aligning the major axis of the resulting, now elliptical, annulus with the major axis of M31. This is the same procedure we used when calculating our global surface brightness profile.

The global and major axis light profiles are shown in Figure 3.3. The localized

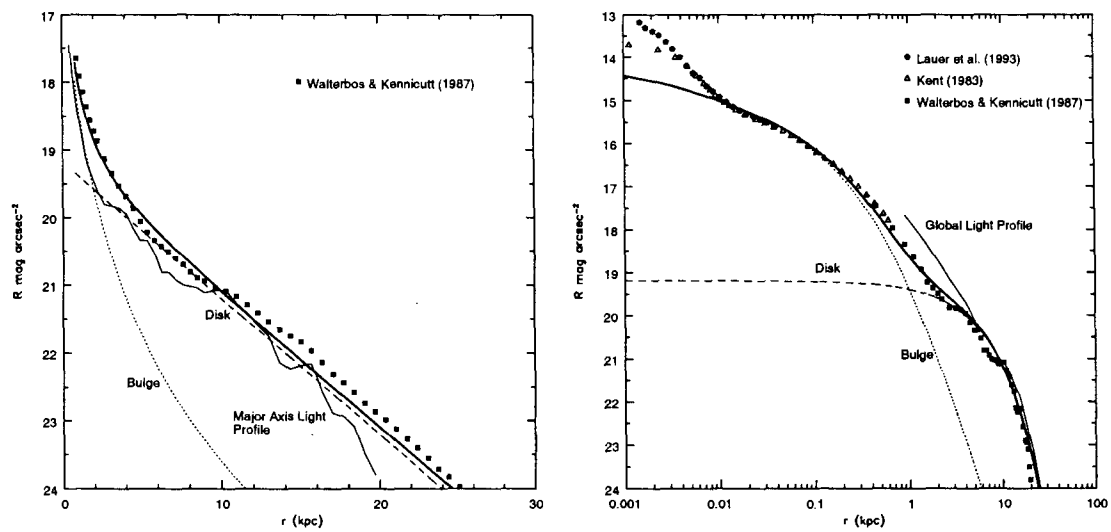

Figure 3.3 *(Left panel)*: The global surface brightness profile of M31. The solid squares represent the data of Walterbos and Kennicutt (1987), corrected as described in the text. The thick solid lines show the results of our best-fit model. The dotted line is the bulge contribution, the dashed line the disk and the thick solid line is the total. For comparison purposes, we juxtapose the observed major axis surface brightness data of Walterbos and Kennicutt (1987) from the right panel as the thin line. *(Right panel)*: The symbols trace the composite, observed M31 major axis surface brightness profile. For comparison, we plot the observed global light from the left panel as a thin solid line. As in the left panel, the thick solid line represents the major axis light profile for our best-fit model, while the dotted and dashed lines represent the contributions.

features can be seen in the right panel (major axis profile) between $r = 1$ kpc and $r = 10$ kpc. In the left panel we plot the global surface brightness profile of Walterbos and Kennicutt (1987). The left panel (global profile) shows how the process of azimuthal-averaging smoothes the effects of localized structures in the disk. One can also see that the major axis surface brightness profile strongly indicates the presence of a stellar nucleus which begins to dominate the light at $r < 0.01$ kpc, which is separate from the bulge (see Kormendy and Bender, 1999). As noted in Chapter 2, we made no attempt to model the nucleus because its mass is too small to affect the masses of the components of our galaxy or the orbits in the halo region. Also mentioned previously, the major axis light profile has a series of prominent bumps and wiggles not present in the global light curve which are due to dust lanes, disk warps, and spiral arms that intersect the major axis. The process of azimuthal averaging minimizes the presence of these features in the global profile.

Our model major axis surface brightness profile is computed as $\mu(r) = \mu_B(0.9r) + \mu_D(r)$, where the disk and bulge surface brightnesses in the R-band are given by

$$\mu_D(r) = \left(\frac{M}{L_R}\right)_D^{-1} \Sigma_0 e^{-r/R_D} \sec(i), \tag{3.1}$$

where $\sec(i)$ accounts for inclination, and

$$\mu_B(r) = 2\left(\frac{M}{L_R}\right)_B^{-1} \int_r^\infty \rho_B(x) \frac{x}{\sqrt{x^2 - r^2}} dx. \tag{3.2}$$

Notice that in computing the disk surface brightness, we sum disk surface brightness at radius r in the disk; however, when computing the bulge surface brightness we sum at $0.9r$. The reason for doing this is to compensate for the fact that in our model the projected distribution of light from our bulge is circularly symmetric while the observed light distribution is ellipsoidal in shape. The factor of 0.9 comes from requiring that the area enclosed by an elliptical isophote at distance r along the major axis is the same as the area of our equivalent circle. This "correction" has the effect

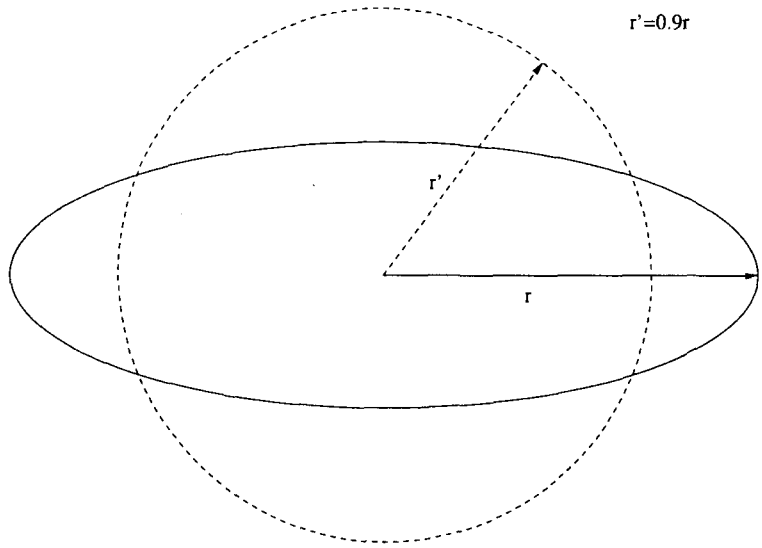

Figure 3.4 The above figure shows how the actual distribution of the light in M31's bulge (elliptical in shape) is mapped onto our circularly symmetric model light profile. The dashed circle represents our circularly symmetric light distribution, while the solid ellipse represents the actual light distribution.

of stretching our circularly symmetric bulge light profile outward. This "correction" is illustrated in Figure 3.4.

The global or average light profile was calculated using the same method as Walterbos and Kennicutt (1987) described earlier. It is computed as $\mu(r) = \mu_B(r) + \mu_D(r)$ where the quantities are now averages. The disk surface brightness in R-band is calculated in the same way as the major axis profile, however the bulge contribution is now averaged over ellipses of infinitesimal thickness. Recall that the ellipse is constructed by rotating a circle by $i = 77°$. It is expressed as

$$\mu_B(r) = 2\Big(\frac{M}{L_R}\Big)_B^{-1} \int_0^{2\pi} \int_r^{\infty} \rho_B(x) \frac{x}{\sqrt{x^2 - r^2}} dx d\phi, \tag{3.3}$$

where $r = x\sqrt{\cos^2\phi + \cos^2 i \sin^2\phi}$ is the distance from the centre to the edge of the ellipse as a function of ϕ, the angle around the ellipse. Here x is the radius of

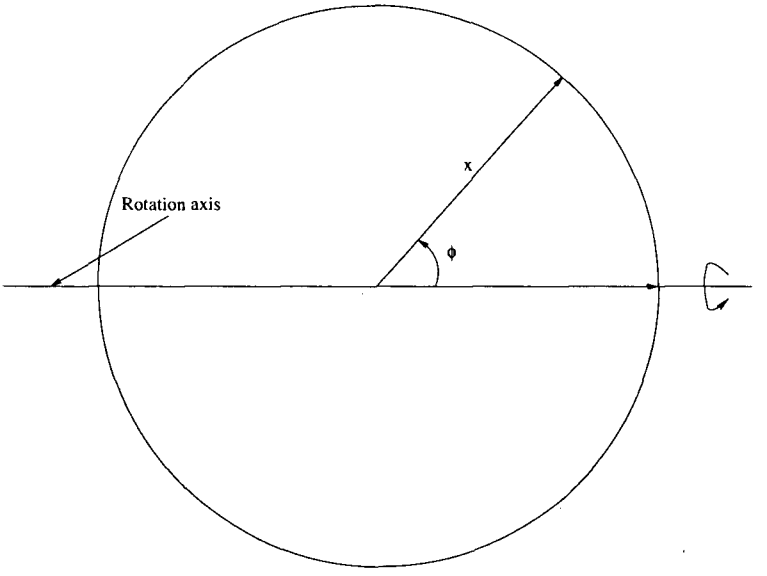

Figure 3.5 The above figure illustrates the first step in calculating the average bulge surface brightness, constructing a circle of radius x. After this circle is constructed it will be rotated by $i = 77°$ around the rotation axis shown above in the direction indicated.

the circle, before rotation. The geometry of this averaging process is illustrated in Figures 3.5 and 3.6

In fitting these two surface brightness profiles (azimuthally-averaged and major axis), we assign an uncertainty of ± 0.1 mag arcsec^{-2} to each data point. The random errors in the data are probably a strong function of radius since they drop with surface brightness, however there are significant systematic errors from zero-point shifts and colour corrections in all parts of the data (Walterbos and Kennicutt, 1987), such that an assumption of a ± 0.1 mag arcsec^{-2} is reasonable.

The global and major axis light profiles are shown in the left and right panels, respectively, of Figure 3.3 for our best-fit M31 mass model. The model agrees with the data over most of the region of interest (excluding the nuclear regions) within 0.2 mag arcsec^{-2}. There is however a seemingly disconcerting systematic offset of

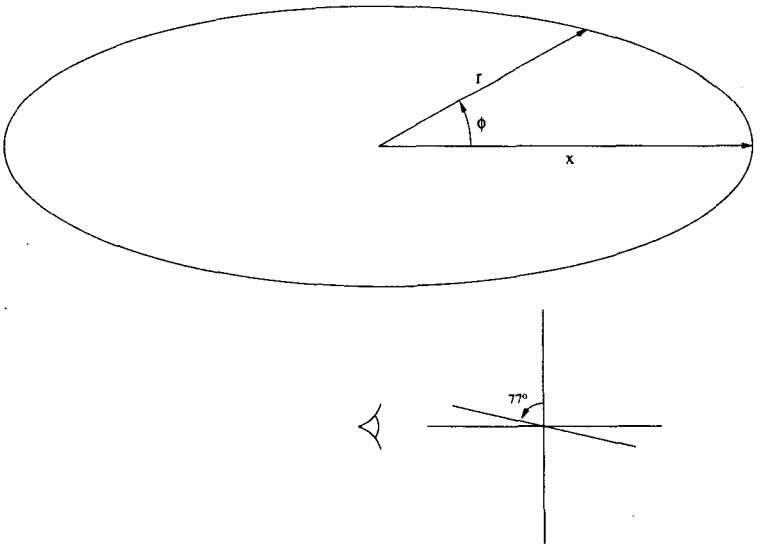

Figure 3.6 The above figure illustrates the circle from Figure 3.5 after it has been rotated 77° into an ellipse. It is clear from the geometry that $r^2 = x^2(\cos^2\phi + \cos^2 i \sin^2\phi)$.

$\sim$ 0.2 mag arcsec^{-2} at $r > 10$ kpc between the model and the data global surface brightness profiles. This offset can be explained by the fact that for $r > 10$ kpc, the *observed* global light profile is brighter than the *observed* major axis profile by as much 0.5 mag arcsec^{-2} at $r = 20$ kpc (Walterbos and Kennicutt, 1987). A trace of the observed major axis and global light profiles are shown in the left and right panels of Figure 3.3 respectively to facilitate comparison. If the disk were infinitesimally thin, perfectly axisymmetric system, and the bulge actually spherically symmetric, the major axis and global surface brightness profiles would be indistinguishable. The observed differences in the light profiles are due to an increased contribution to the global light profile from the bulge due to its ellipsoidal shape, the warpage in the disk, and its actual finite thickness. Our mass model does not account for these additional features in the profiles, therefore we do not expect to be able to model this offset. Instead, our best-fit model "splits the difference" and settles in between the

two profiles.

3.2 Disk Rotation Curve

The rotation profile of M31's disk is shown in Figure 3.7. As with the photometric data, there is quite a large amount of optical and radio observations of the rotation data for the M31 disk. We chose to use the smoothed, composite rotation curve of Widrow et al. (2003), which was based on the results of Kent (1989) and Braun (1991). Kent (1989) obtained velocities for 30 HII emission regions along the major axis of the galaxy in the range of 6-25 kpc. The measurements of Braun (1991) were of neutral hydrogen within M31's gaseous disk. These measurements were made out to a radius of $\sim$ 30 kpc. Widrow et al. (2003) neglected Braun's data within 2 kpc of M31's centre due to possible distortion from the bar-like triaxial bulge. Measurements beyond $\sim$ 20 kpc were only made for spiral arm segments on only one side of the galaxy, therefore this data was also not included in the smoothing process. A Gaussian kernel was used in the smoothing process with a width equal to the spacing between the points (see Widrow et al., 2003, Figure 1 for the rotational velocity data and Figure 3 for the velocity dispersion). The individual data points from the two authors were weighted by the error bars quoted in the literature and another error associated with the spread in the data. These two errors were added in quadrature.

The rotational velocity for our different components were calculated using the spherical approximation $v_c^2 = GM/r^2$. The black hole, bulge, halo, and spherical disk components are simple to calculate using this relation, however the rotational velocity for the flattened disk is calculated in the plane of the disk and is given by

$$V_{cD}^2(r) = 4\pi G\Sigma_0 R_D y^2[I_0(y)K_0(y) - I_1(y)K_1(y)], \tag{3.4}$$

where $y = r/2R_D$, I_0, I_1 are modified Bessel functions of the first kind, and K_0, K_1 are

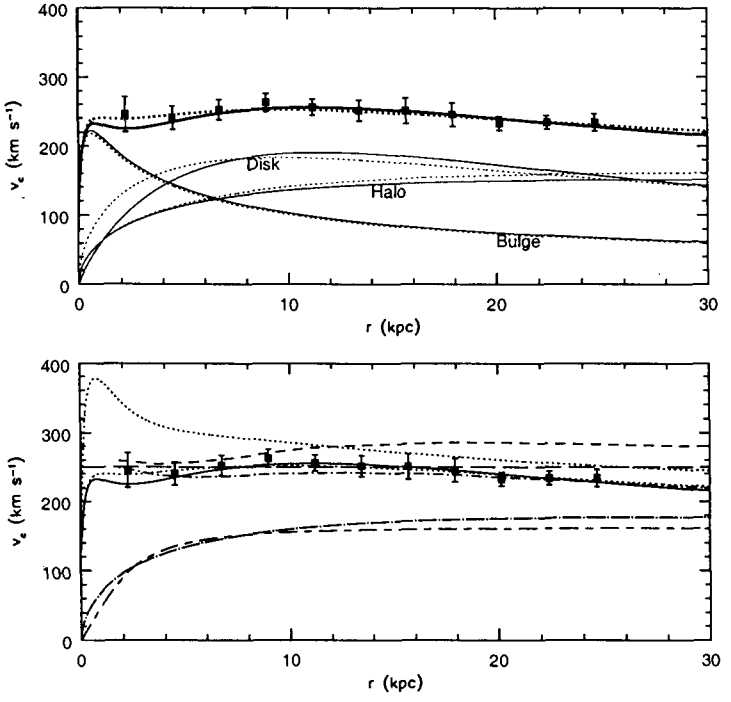

Figure 3.7 The upper panel compares our best-fit flattened disk model rotation curve (thick solid line) against the observed M31 disk rotation profile. The thin solid lines represent the contributions from the bulge, disk, and halo. Also shown is the best-fit model for our spherical disk (the thick dotted line is the total, the light dotted lines, the contributions from the components). The spike in the curves at $r = 0$ is due to the effect of the black hole. The bottom panel compares these best-fit rotation curves (solid and dotted lines) against the corresponding rotation curves of the singular isothermal sphere model - see Chapter 4 (long dashed line), the toy NFW and logarithmic models of Ibata et al. (the two lower dot-dashed and short dash-long dashed lines, respectively), as well as the two axisymmetric models of Ibata et al. based on the mass model of Klypin et al. (2002) (the two upper dashed and dot-dashed lines), as well as the bulge-disk-halo model of Bekki et al. (2001) adopted by Font et al. (2005) (dotted line near the top of the panel).

modified Bessel functions of the second kind. Compare this to the rotational velocity of the spherical disk

$$V_{cD,sp}(r) = \frac{2\pi G\Sigma_0 R_D(R_D - e^{-r/R_D}(r + R_D))}{r}. \tag{3.5}$$

The upper panel of Figure 3.7 shows the total disk rotation curve for our best-fit axisymmetric model (thick solid curve) as well as the contributions for the bulge, disk, and halo (light solid curves). This model is in excellent agreement with the observations. Also shown in the same panel are the results of our best-fit spherically symmetric model where we have replaced the flattened disk with our toy exponential spherical disk. It can be clearly seen in the upper panel that the spherical disk component peaks in its circular velocity before the flattened disk component and in fact the spherical disk is more massive than the flattened disk (see Table 3). This can be understood by substituting the flattened disk parameters in place of the best-fit parameters for the spherical case, the result being that the circular velocity for $r \gtrsim 0.8R_D \approx 4$ kpc would have been lower than the observed profile. Therefore to compensate, the fit in the spherically symmetric model converges to a more massive disk and slightly more massive halo. The more massive spherical disk raises the total rotation curve for $r < 5$ kpc. In almost all other ways the two model curves are nearly identical, and the toy spherical model agrees just as well with the observations as the more realistic axisymmetric model.

3.3 Bulge Velocity Dispersion

Figure 3.8 shows the projected bulge velocity dispersion profile along the bulge major (PA=45°) and minor (PA=135°) axes. The former is plotted in the upper panel while the latter is shown in the lower panel. The filled squares and triangles with error bars show the observed velocity dispersion profile used in our fitting procedure. As with the rotation profile, these data points represent the smoothed profile of Widrow

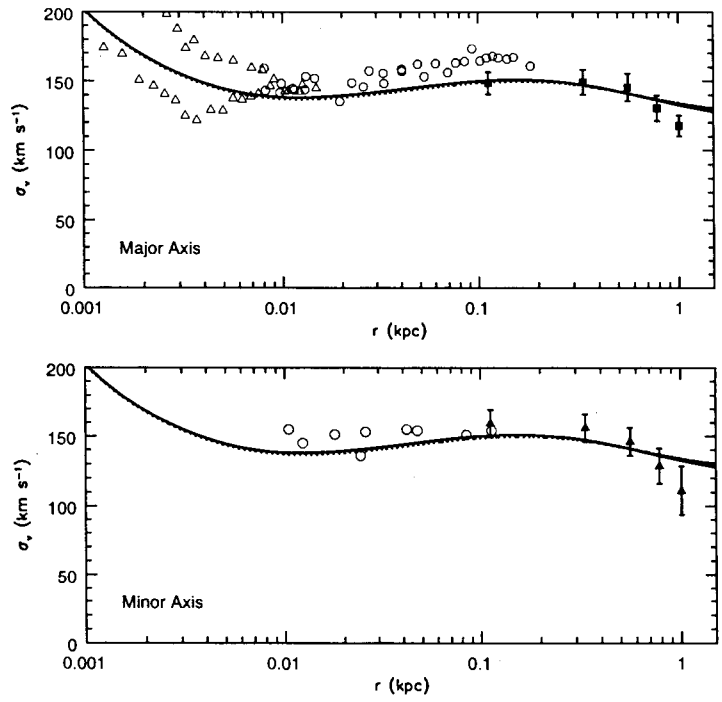

Figure 3.8 The upper and lower panels show the measured bulge velocity dispersion along the bulge major and minor axis, respectively. The solid curve represents the best fit mass model for our axisymmetric model. The dotted line is the best fit model when we replace the axisymmetric disk with a spherical disk. The filled squares and triangles represent the major and minor axis data, respectively, of McElroy (1983) as smoothed by Widrow et al. (2003). This was the only data used as constraints on our model. Also plotted are the major and minor axis velocity dispersion data of Kormendy (1988) (open circles) and the major axis data of Kormendy and Bender (1999) (open triangles). These two data sets were not included as constraints on our models and are only shown here for illustrative purposes. The upturn in the curves at ~ 0.01 kpc is due to the influence of the central nucleus and the black hole.

et al. (2003) which is based on data from McElroy (1983) (see previous section for a brief description of the smoothing process). McElroy (1983) took velocity and velocity dispersion measurements of the stellar component of M31's bulge using the KPNO 1 92 cm telescope with the White Spectrograph and the Ritchey-Crétien (RC) Spectrograph at the Cassegrain focus of the KPNO Mayall 4 m telescope. Due to concern about the dynamical effect of bulge rotation and/or contamination from the disk, we show data only out to 1 kpc. Also included in the plot for comparison purposes are data points at smaller radii from Kormendy (1988) (open circles) and Kormendy and Bender (1999) (open triangles). Kormendy (1988) collected data on the stellar rotation velocities and velocity dispersion for the inner regions of M31 using the Canada-France-Hawaii Telescope and the Herzberg spectrograph. The data from Kormendy and Bender (1999) were also collected using the CFHT and Subarcsecond Imaging Spectrograph. The stellar kinematics were measured using spectra at the Ca infrared triplet lines. These data points extend the velocity dispersion profiles well into the nucleus of M31. There is a slightly disconcerting aspect of the major axis plot however. In the region where the Kormendy (1988) data overlaps with the McElroy (1983) observations the plot indicates that the Kormendy (1988) data is $\sim$ 15% higher than the McElroy (1983) data. This offset may partly be due to McElroy (1983) and Kormendy (1988) using slightly different values for the PA of the bulge major axis.

In keeping with our basic assumption of a spherically symmetric bulge we have made three additional simplifications in computing the model velocity dispersions. These assumptions are:

1. The bulge velocity dispersion is isotropic

2. The disk potential in the central 1.2 kpc can be approximated by that of a spherical disk

3. The bulge rotation can be neglected. Our primary motivation for doing this is to remain consistent with our assumption of a spherical bulge, and also the

fact that the bulge rotates at a small level relative to its velocity dispersion. In addition, McElroy (1983) noted that there were several asymmetries in the rotation curves on the two sides of the putative axis of rotation as well as along various different position angles. These asymmetries suggest that determining a mean bulge rotation velocity is not straightforward, which further encourages us to neglect it.

With these assumptions the true (unprojected) bulge velocity dispersion is

$$\sigma_r^2 = \frac{1}{\rho_B(r)} \int_r^\infty \rho_B(r') \frac{\partial \Phi_{tot}}{\partial r'} dr'. \tag{3.6}$$

The observed profile, however, is a luminosity-weighted projected velocity dispersion. Our model must reflect this, therefore our *projected* profile is (Simien et al., 1979; Kent, 1989)

$$\sigma_p^2 = \frac{1}{\mu_B(r)} \left(\frac{M}{L_R}\right)_B^{-1} \int_r^\infty \rho_B(r') \sigma_r^2(r') \frac{r'}{\sqrt{r'^2 - r^2}} dr', \tag{3.7}$$

where $\mu_B(r)$ is the bulge surface brightness profile given in Equation 3.2. Since our model isophotes are circular in shape whereas the actual bulge isophotes are elliptical and the projected velocity dispersion is luminosity weighted, we ought to rescale our profiles so that along the major axis, $\sigma_p(r)$ is stretched out by $\sim 10\%$ and compressed by the same amount along the minor axis, as we did in computing the major axis light profile. However, we omit this step because $\sigma_p(r)$ is so flat the rescaling would have a negligible effect.

The solid curves in the two panels show the velocity dispersion for our best-fit axisymmetric mass model, while the dotted curves show the dispersion profile for our spherically symmetric toy mass model. It is clear from Figure 3.8 that our two best-fit results match fairly well to the data actually used to constrain our model. Both our models and the data show a decline in the velocity dispersion profile towards increasing radii beyond $r = 0.2$ kpc, however the decline in our models is not as steep

as indicated by the smoothed McElroy (1983) data. More interestingly, although our mass models were not constrained by the Kormendy (1988) and Kormendy and Bender (1999) data, they still reproduce the gentle decline towards the centre inward of 0.1 kpc, the trough at ~ 0.01 kpc, and the subsequent rise into the centre which is due to the effect of the black hole and central nucleus.

Comparing our results to those obtained by others with more sophisticated assumptions about the bulge geometry and velocity distribution, we find that our results are not significantly affected by our three assumptions listed above, especially the second and third. We base this on the discussions found in Simien et al. (1979) and Kent (1989). The former demonstrates that the impact of bulge rotation on the determination of $\sigma_p^2(r)$ for $r < 0.3$ kpc is negligible. Between 0.3 and 1.0 kpc the rotation profile of the bulge rises from $V_{c,B} \sim 0.3\sigma_p$ to $0.5\sigma_p$. It is, therefore, possible that with increased support from rotation that the observed σ_p is allowed to drop off while in our model, σ_p must remain high in order to maintain pressure support. Although this argument sounds reasonable the results of Kent (1989) do not support it. The model constructed in that work assumed, like in our model, an isotropic bulge velocity dispersion, however, he assumed an oblate spheroidal model for the mass distribution of the bulge, which differs from our model. He also took into account the axisymmetric nature of the disk potential, and allowed for bulge rotation. The velocity dispersion from Kent (1989) was systematically $\sim 10\%$ higher than ours, which we attribute to the fact that he used the data of Kormendy (1988) in addition to that of McElroy (1983). Also, his major and minor axis velocity dispersions are nearly the same for $r < 1$ kpc, and the shape of his dispersion profile agrees well with ours. It is also worth noting that the Kent model profiles do not decline as sharply as the observed profile, despite his taking into account the geometry and bulge rotation. Given these considerations we feel justified in having made our simplifying assumptions to the extent that we have excellent overall agreement with the more rigorous calculations of Kent (1989). A possible clue to the origin of the steeper than predicted decline in

σ_p^2 may lie in the different rates at which the major and minor axis dispersion profiles fall off. This difference between the two profiles has been noted by both Simien et al. (1979) and Kent (1989) as indicating velocity anisotropy.

3.4 Total Mass Estimates from the Intermediate and Outer Halo Regions

The final set of constraints we consider for our model are on the mass constraints of the system from dynamical studies of globular clusters, planetary nebulae, and M31 satellites. A number of studies have used these tracers to estimate the total mass profile of M31 in the intermediate and outer regions of the halo. However, many of these estimates do not contain a well-motivated error bar, which is needed for our fitting procedure; many studies have simply propagated the observational errors through their mass estimator and ignored the larger statistical errors altogether. For constraining our M31 mass model we use the results of Evans and Wilkinson (2000) and Evans et al. (2000), who use Bayesian statistics to make their mass estimates. This type of statistics makes estimates of parameters of a distribution based on the observed distribution. One begins with a "prior distribution" which can be based on any type of observation that can be made about the distribution. By combining the observed and prior distributions gives what is called the posterior distribution. The mode of this distribution is the parameter estimate.

Evans and Wilkinson (2000) made an estimate of the mass of M31 using a collection of planetary nebulae and globular cluster data. As mentioned above they use Bayesian statistics to make their mass estimate. The data used for their estimate are found in their Tables 2 and 3. They model the planetary nebulae and globular cluster data using the distribution function of Osipkov-Merritt (see their Equation 8). They estimate that $M(< 31 \text{ kpc}) = (2.8^{+2.4}_{-1.2}) \times 10^{11}$ $M_\odot$ form the planetary nebulae

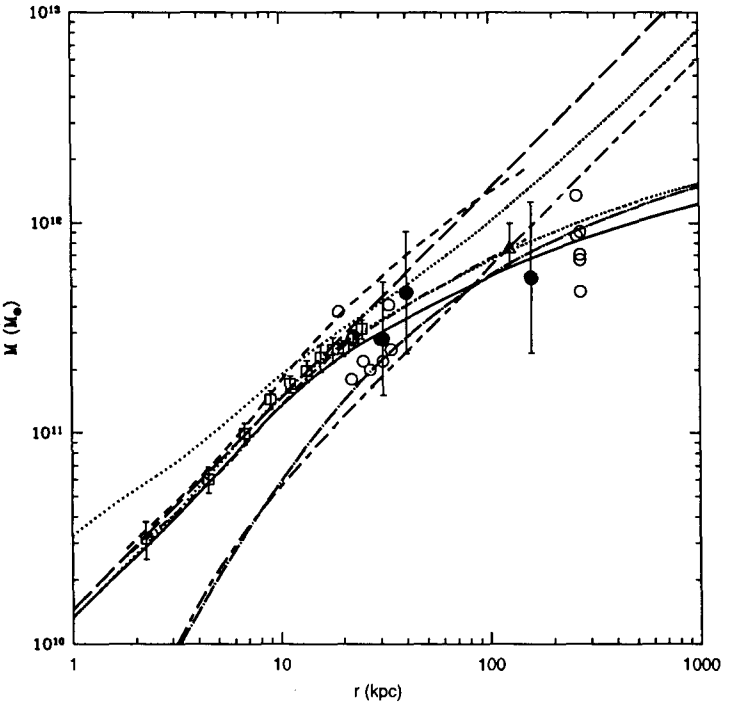

Figure 3.9 A comparison of the mass profiles for different models: Our best-fit axisymmetric model (solid line), our best-fit spherical model (dotted line), the singular isothermal model - see Chapter 4 (long dashed line), the toy NFW and logarithmic models of Ibata et al. (2004) (the two lower dot-dashed and short dash-long dashed lines, respectively), the two axisymmetric models of Ibata et al. (2004) based on the mass model of Klypin et al. (2002) (the two upper dashed and dot-dashed lines), as well as the bulge-disk-halo model of Bekki et al. (2001) used by Font et al. (2005) (dotted line near top right corner). The three solid circles represent the mass estimates used as constraints on our models. The first two solid circles are mass estimates from Evans and Wilkinson (2000), while the last circle is a mass estimate based on M31 satellite galaxies from Evans et al. (2000). The open squares represent the mass from the previous rotation curve plot computed using the singular isothermal sphere approximation. The open triangle represents an estimate of the mass within 125 kpc derived by Ibata et al. (2004) while the open circles represent mass estimates from many sources which are summarized in Table 6 of Evans and Wilkinson (2000). None of the mass estimates shown as open symbols were used as constraints on our mass model.

data and $M(< 40 \text{ kpc}) = (4.7^{+3.4}_{-2.3})\times 10^{11}$ $M_\odot$ from the globular cluster data. The two radii, 31 kpc and 40 kpc, were chosen by taking the median projected radius from their data sets and converting it to a three-dimensional radius by multiplying by a deprojection factor of $\pi/2$. Evans and Wilkinson (2000) argue that of these two estimates, the mass estimate based on the globular clusters is more robust because these tracers are more uniformly distributed while the planetary nebulae tend to be concentrated in two regions near the optical disk.

To estimate the mass further out in the halo, Evans et al. (2000) analyzed the data for the dwarf spheroidal companions of M31. The data came the HIRES and LRIS spectrographs on the Keck Telescope. The HIRES data came from the work of Côté et al. (1999) and the LRIS from Guhathakurta et al. (2000). To model the satellite galaxies Evans et al. (2000) assume that the halo of M31 is spherically symmetric and its density and potential are given by simple analytic expressions. The satellite galaxies are modelled using the same Osipkov-Merritt (see Equation 8 Evans and Wilkinson, 2000). We use the results from their analysis to estimate the mass at 158 kpc, which is the radius of the median object (And II) of 13 M31 satellites, *excluding* Pegasus and IC 1613. These galaxies were excluded because they appear to be outside the M31's virial radius and therefore should not be included in an analysis that assumes statistical equilibrium. Our mass estimate was made by averaging the results of their two velocity distributions, and making a small correction from their stated total mass to $M(<158 \text{ kpc})$ using their mass profile. The resulting mass estimate is $M(< 158 \text{ kpc}) = (5.5^{+7.1}_{-3.1})\times 10^{11}$ $M_\odot$. For each of the three halo mass estimates, the given confidence intervals were converted to approximate symmetrical error bars in $\log(M)$ for use in our χ^2 fit.

Figure 3.9 shows the above three mass estimates as filled circles. These are the values that we use to constrain our mass models. The open squares that extend from ~ 2 to ~ 30 kpc trace the mass estimates based on the rotation curve data which were computed using the spherical approximation $v_c^2 = GM/r$. The open triangle

at 125 kpc represents the mass estimate derived by Ibata et al. (2004) from their preliminary analysis of the dynamics of the giant southern stream. The final set of symbols, the open circles, represent different mass estimates from a number of different studies dating back from 1970. The estimates and the appropriate citations can be found in Table 6 of Evans and Wilkinson (2000). Note that none of the open data points are used as constraints on our mass model. Our mass model was calculated as the sum of the black hole, bulge, disk, and halo, i.e. $M(r) = M_{BH} + M_B(r) + M_D(r) + M_H(r)$. The black hole mass is constant as discussed in Chapter 2 while the rest of the mass components are given by Equations 2.2, 2.5, and 2.9. The rotation curves resulting from our two models are nearly indistinguishable (see Figure 3.7), however, Figure 3.9 shows that the toy spherical disk model (dotted curve) passes through these points while the flattened disk model (solid curve) lies below, which clearly indicates the importance of taking disk flattening into account.

Also shown in Figure 3.9 are the results of our best-fit axisymmetric (solid curve) and spherical models (dotted curve). Both curves are in excellent agreement with the three data points used as constraints and in good agreement with the entire slew of mass estimates shown in the figure. The best-fit parameters for these mass models are listed in Table 3.

Chapter 4

Converging on a Physically Plausible Mass Model

In Chapter 3 we presented our best-fit values for the parameters describing our two M31 mass models (Table 3) and compared our model results against the observations. It is clear from our discussions that the two models do a remarkably good job matching the most important features in the observed profiles. Despite this success, we find that there are aspects of the models that lead us to question whether the best-fit solutions are actually physically reasonable. For example, the high value of the mass-to-light ratio of the axisymmetric disk at $M/L_R = 5.5$ (uncorrected for internal or foreground extinction) is more indicative of old stellar populations. Also, the normalized fraction of "galactic" baryons in both the spherical and axisymmetric models is > 1. Figure 3.7 shows that the disk component of our mass model dominates the rotation curve over much of the inner 30 kpc. This domination of the rotation curve by the disk is a common feature of high disk mass models and suggests that the model is susceptible to a bar instability. This instability can be suppressed by an extended halo or a bulge that dominates the dynamics of the inner regions of the galaxy. In their study of various mass models of M31, Widrow et al. (2003) found that disks

tended to become unstable in the neighbourhood of $M_D \simeq 8 \times 10^{10}$ $M_\odot$. Models in this mass range show signs of spiral and bar-like structures. Given that spiral structure in the disk and a triaxial bulge are both present in M31, Widrow et. al. state that $M_D = 8 \times 10^{10}$ $M_\odot$ should not be taken as an upper bound on the disk but a region of parameter space that may give rise to non-axisymmetric structures. Based on these discussions and given the fact that our disk mass is $M_D = 11.8 \times 10^{10}$ $M_\odot$ ($\sim$ 1.5 times greater than Widrow et. al.'s "upper limit") we expect that a disk in a fully realistic galaxy model with properties similar to our best-fit case would be susceptible to bar instability. Given these concerns, we reconsider our best-fit model. Our first step is to investigate the solution space in the neighbourhood of the best-fit and then to introduce the disk mass-to-light ratio as an additional constraint. The hope is that this additional constraint will confine the region of statistically acceptable solutions to one that is also physically acceptable. The resulting "constrained" best-fit model is described in Table 4.2.

4.1 Allowed Regions of Parameter Space

There is a difficulty in modelling the mass distributions in galaxies in that efforts are hampered by degeneracies between the various parameters. Specifically in our case we expected a linked bulge-disk-halo degeneracy where the disk and halo played off against one another to match the M31 rotation curve, while the bulge and disk did the same with the respect to the dynamics of the inner regions. However, our use of both photometric and kinematic data greatly reduces the number of degrees of freedom in our model.

Of the eight parameters discussed in Chapter 3, two—the mass-to-light ratios of the disk and bulge—are not really independent variables. Their appearance in Equations 3.1 and 3.2 are as multiplicative factors which relate the disk and bulge mass profiles to the M31 light profile. The consequence of this is that once the

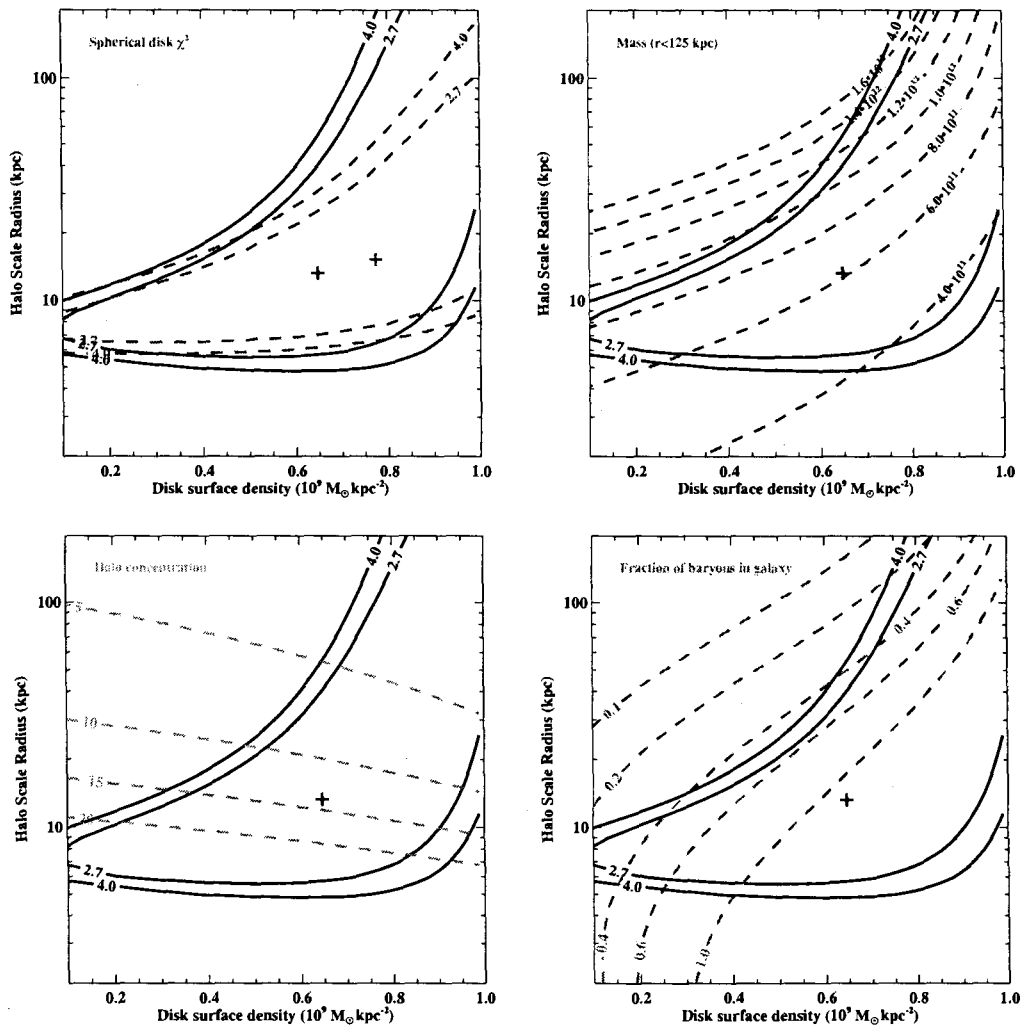

Figure 4.1 The above four panels show the $\Delta\chi^2$ =2.7, 4.0 contours for our axisymmetric model (solid lines in all panels). The best-fit solution is indicated by cross marks (see Table 3). The upper left panel shows the contours for the spherical disk (dashed curves) superposed on those for the flattened disk case. The shapes of the two sets of contours are broadly similar though the spherical disk contours and the best-fit solution are shifted towards more massive disk and halo. The upper right-hand panel superposes lines of constant total mass within 125 kpc (dashed lines). The lower left-hand panel superposes lines of constant halo concentration (dashed lines). The lower right-hand panel superposes lines of constant baryon fraction (dashed lines) as defined in the text

bulge and disk parameters (M_B, r_B and Σ_0, R_D, respectively) are determined the corresponding mass-to-light ratios are fixed by the M31 surface brightness profiles. The scale radii of the bulge and disk are also determined from the light profiles fairly precisely to 0.61 kpc and 5.4 kpc, respectively. Therefore, after doing the surface brightness fit, we fix r_B and R_D to these values which removes them as degrees of freedom in the subsequent fitting routine.

In addition we find that the two parameters which describe the halo, δ_c and r_H, are coupled so strongly that if all the other parameters are already fixed, setting one of the halo parameters effectively sets the other. The main reason for this behaviour is the small error bar on the rotation curve data points, which tightly constrains the contribution in that region. The constraints on the outer halo are not as strong as can be seen in Figure 3.9.

Moreover, the solutions with the lowest χ^2 lie on a thin plane corresponding to a specific set of bulge masses M_B. The values of this parameter are remarkably robust in that large changes in the other parameters result in a $< 10\%$ change in the bulge mass. Similar behaviour was also noted by Widrow et al. (2003) who described the neighbourhood of their best-fit solution as a "trough [in the M_D-M_B plane] running parallel to the M_D axis."

With these relationships between the parameters and the best-fit solutions we are left with only two parameters, Σ_0 and one of the two halo parameters, to span most of the available parameter space. Figure 4.1 shows the location of χ^2 contours in the Σ_0-r_H plane. Contour levels of $\Delta\chi^2 \equiv \chi^2 - \chi^2_{\rm min} = 2.7$, and 4.0 are shown corresponding to approximately 68% and 90% confidence intervals for two parameters. If we were able to fix one of the two parameters (as we do later with Σ_0 using the mass-to-light ratio of the disk as a further constraint) then the same contours map out the 90% and 95% confidence intervals for the remaining parameter (Press et al., 1992). It is clear from the plot that the area of the plane that produces acceptable fits is quite large, however the transverse width of this allowed region is small in the

other dimensions of parameter space. The shape of the contours shows that there is a degeneracy between the disk and the halo components. The trade off between these two components has been a long-standing problem in fitting models to galaxy rotation curves (Dutton et al., 2003). The contours extend from regions of "maximum disk" models in the upper right to regions where the disk is only a minor contributor to the rotation curve in the lower left of the plot.

The upper left panel of Figure 4.1 superposes the contours for the axisymmetric and spherically symmetric models. Although there are differences in the location of the best-fit solution and in the details of the shape of the contours between the two models, overall they quite are similar. The primary difference between the two cases is the shift to higher disk surface densities for the spherical disk for reasons discussed in Chapter 3.2.

The three remaining panels in Figure 4.1 focus only on the axisymmetric case and juxtapose tracks for different physical characteristics of the mass models alongside the contours. The upper right panel shows lines of constant mass within 125 kpc superposed on the contour map. The best-fit solution for the axisymmetric model lies on the line for $M(< 125\,\mathrm{kpc}) = 6.1 \times 10^{11}\,\mathrm{M}_{\odot}$. As mentioned earlier in this thesis, Ibata et al. (2004) in their preliminary analysis of the dynamics of the giant southern stream found a lower limit on the mass within 125 kpc of $M(<125\ \mathrm{kpc}) = 5.4 \times 10^{11}\ \mathrm{M}_{\odot}$. This constraint on the mass excludes the lower right region of the 99% confidence region, along with the entire lower right corner of the Σ_0-r_H plane, thus reducing the region of allowed parameter space.

The lower left panel shows a plot where we have superposed lines of constant halo concentration C_{200} on the contour map. It is important to note that our notation emphasizes the fact that we define the virial radius as the radius enclosing a mean density that is 200 times the critical density, which is in contrast to some other authors. Studies using numerical simulations suggest that in the absence of baryons, $\sim 10^{12}\ \mathrm{M}_{\odot}$ halos have concentration parameters of $C_{200} \approx$ 7-14 (Bullock et al., 2001;

Wechsler et al., 2002; Dolag et al., 2004). The effect of including baryons, if anything, will tend to make the halos more concentrated due to gravitational compression of the inner regions of the halo. This follows the expected cooling and pooling of the baryons at the centre of the halos (Blumenthal et al., 1986; Klypin et al., 2002). However, heating of the dark matter by the gas during the process of galaxy formation (Mo and Mao, 2004) and by a bar in the central disk (Weinberg and Katz, 2002) may partially counteract the effect of compression of the dark matter. For these reasons we decide to use $C_{200} > 7$ as a lower limit on the effective dark halo concentration. With this condition, the upper third of the Σ_0-r_H is excluded, which includes some of the 99% confidence region.

The final panel in the lower right corner superposes the contours of the fraction of baryons within the virial radius R_{200} that are "galactic", i.e., within the bulge and the disk component: $f_{gal} = \Omega_m(M_B + M_D)/(\Omega_B M_{200})$. We have assumed in computing this quantity that all the matter in the bulge and disk is purely baryonic. This assumption has long been debated even in the case of the Milky Way, however, the bulge and disk are probably not *dominated* by dark matter so that the error from making this assumption is probably small. Since this fraction must be less than unity, most of the lower right half of the Σ_0-r_H plane is excluded. For $\Sigma_0 > 4.5 \times 10^8$ $M_\odot$ kpc^{-2}, this condition is stricter than the constraint on the mass within 125 kpc and in fact, excludes our best-fit solution. These different constraints are shown together in Figure 4.2. In combination with the $\Delta\chi^2$ contours, these constraints severely restrict the region of allowed solutions.

4.2 Disk Mass-to-Light Ratio

Now that the allowed region of physically plausible models has been identified, we require an additional constraint that can be used to identify a unique best-fit solution from within this allowed region. We adopt the disk mass-to-light ratio as the

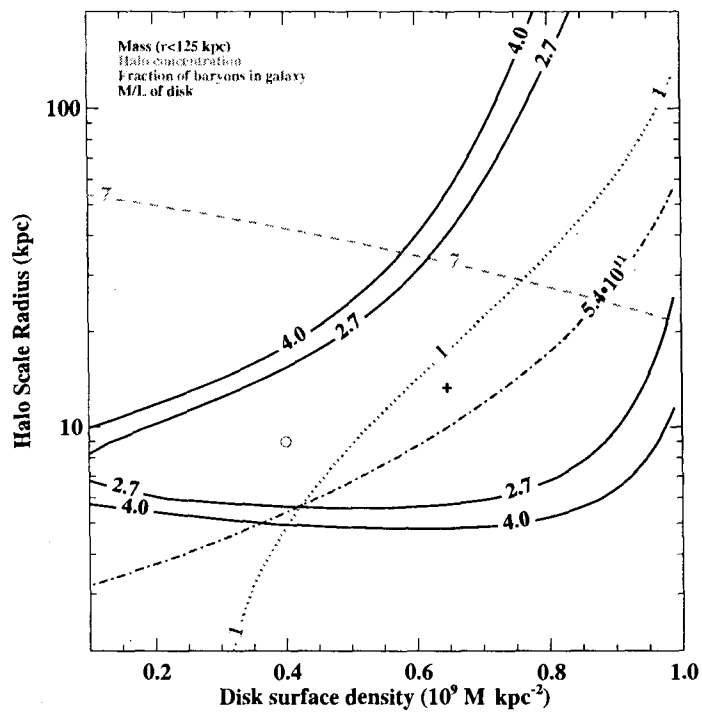

Figure 4.2 The above plot again shows the $\Delta\chi^2$ =2.7, 4.0 contours for our axisymmetric model (solid lines), however, we have also combined, for clarity, the three critical demarcations from the panels in Figure 4.1 (see text). We assert that the allowed region for physically plausible solutions is the section of the $\Delta\chi^2$ =1.0 island that is bounded at the top by $C_{200} = 7$ (dashed curve) and to the right by $f_{gal} = 1$ (dashed curve). Additional lines on the plot correspond to $M(< 125 \text{ kpc}) = 5.4 \times 10^{11}$ (dot-dashed curve) and disk mass-to-light ratio (uncorrected for extinction) of $(M/L_R)_D$ = 3.3 (open circle). Our constrained, best-fit, physically plausible solution (Table 4.2) is show as an open circle on the $(M/L_R)_D = 3.3$ line.

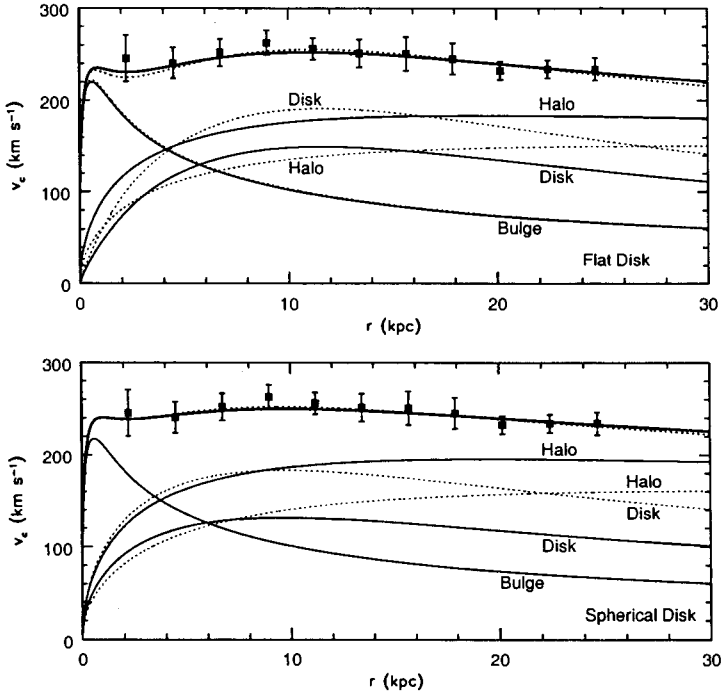

Figure 4.3 Rotation profile for the best-fit constrained $[(M/L_R)_D = 3.3]$ model (solid curves in both panels) juxtaposed against the results for our previous unconstrained best-fit model (dashed curves). The results for the axisymmetric and spherical disks are shown in the upper and lower panels, respectively. The thick lines show the total rotation profile while the thinner lines show the contributions from the different components.

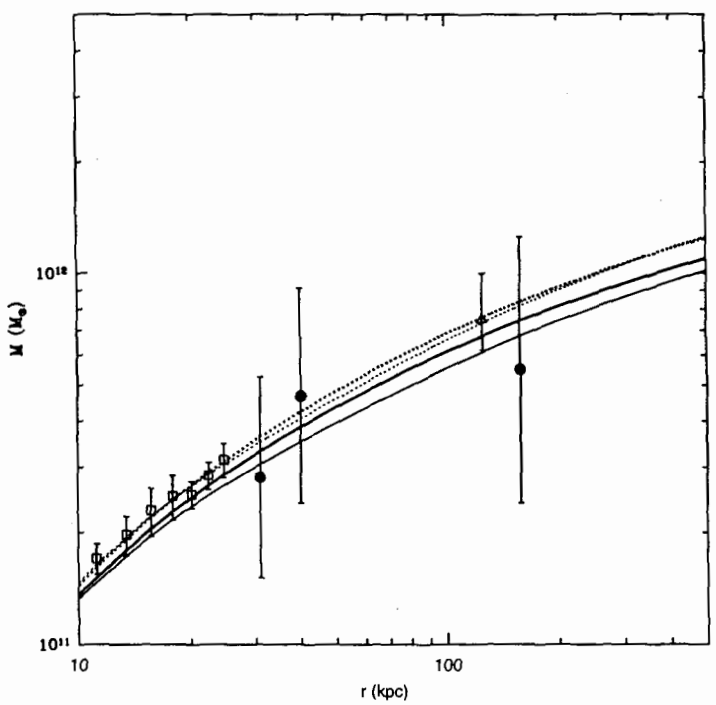

Figure 4.4 The thick lines show the mass profiles for the axisymmetric (solid) and spherically symmetric (dotted) best-fit constrained $[(M/L_R)_D = 3.3]$ models, for $r > 10$ kpc. For comparison, the thin lines show the results for the unconstrained case.

Table 4.1 M31 Mass Model Parameters for Best-fit Axisymmetric and Spherical Cases subject to $(M/L_R)_D$=3.3 constraint

Parameter	Symbol		Axisymmetric Model	Spherical Model
Black Hole Mass	M_{BH}	(10^7 $M_\odot$)	5.6	5.6
Total Bulge Mass	M_B	(10^{10} $M_\odot$)	2.7	2.7
Total Disk Mass	M_D	(10^{10} $M_\odot$)	7.3	7.3
Total Mass inside 125 kpc	$M(< 125$ kpc)	(10^{11} $M_\odot$)	6.8	7.6
Virial Mass	M^*_{200}	(10^{11} $M_\odot$)	8.0	9.1
	M^*_{100}	(10^{11} $M_\odot$)	8.7	10.0
Bulge Scale Radius	r_B	(kpc)	0.61	0.61
Disk Scale Radius	R_D	(kpc)	5.4	5.4
Halo Scale Radius	r_H	(kpc)	9.0	9.2
Virial Radius*	r_{200}	(kpc)	189.4	198.3
	r_{100}	(kpc)	244.5	256.0
Halo Density Parameter	δ_c	(10^4)	25.7	27.7
Halo Concentration Parameter	$C_{200} \equiv r_{200}/r_H$		21.1	21.6
Bulge M/L**	$(M/L_R)_B$		3.3	3.2
Disk M/L**	$(M/L_R)_D$		3.3	3.3
Disk Central Surface Density	Σ_0	(10^8 $M_\odot$ kpc^{-2})	4.0	4.0
Maximum Rotation Velocity	$V_{c,max}$	km s^{-1}	250.7	249.4
Fraction of "galactic" baryons	$\Omega_m(M_B + M_D)/(\Omega_b M_{200})$		0.73	0.63

* We define M_Δ as the mass enclosed with the sphere of radius R_Δ such that the mean density inside is $\Delta\rho_c$, where $\Delta = 100$ or 200 and $\rho_c = 277.72h^2$ $M_\odot$ kpc^{-2} is the present-day critical density.

** The quoted M/L ratios are based on luminosities that have *not* been corrected for internal or foreground extinction.

Table 4.2 Stellar M/L as a function of colour

	Colour					
	B−V	B−R	V−I	V−J	V−H	V−K
a_B	−0.994	−1.224	−1.919	−1.903	−2.181	−2.156
b_B	1.804	1.251	2.214	1.138	0.978	0.895
a_V	−0.734	−0.916	1.476	1.477	1.700	1.683
b_V	1.404	0.976	1.747	0.905	0.779	0.714
a_R	−0.660	−0.820	−1.314	−1.319	−1.515	−1.501
b_R	1.222	0.851	1.528	0.794	0.684	0.627
a_I	−0.627	−0.768	−1.204	−1.209	−1.383	−1.370
b_I	1.075	0.748	1.347	0.700	0.603	0.553
a_J	−0.621	−0.724	−1.040	−1.029	−1.151	−1.139
b_J	0.794	0.552	0.987	0.505	0.434	0.396
a_H	−0.663	−0.754	−1.030	−1.014	−1.120	−1.108
b_H	0.704	0.489	0.870	0.442	0.379	0.346
a_K	−0.692	−0.776	−1.027	−1.005	−1.100	−1.087
b_K	0.652	0.452	0.800	0.402	0.345	0.314

additional constraint on our mass models.

Bell and de Jong (2001) used simplified spectrophotometric spiral galaxy evolution models to study variations in stellar mass-to-light ratios within galaxies. They found a strong correlation between the stellar M/L and the optical colours of the integrated stellar populations. This correlation is robust to uncertainties in stellar population and galaxy modelling including modest bursts of star formation. The relationship between the M/L and the colour is given by

$$\log_{10}(M/L) = a_\lambda + b_\lambda \text{Colour}, \tag{4.1}$$

where a_λ and b_λ are constants determined from fits to the data. They vary depending on the wavelength band and the colour. The stellar M/L as a function of colour is given in Table 4.2 taken from Table 1 of Bell and de Jong (2001).

As noted previously, the disk mass-to-light ratio of $(M/L_R)_D = 5.5$ for our best-fit model is too high. An estimate for the uncorrected disk mass-to-light ratio can be obtained using the mean luminosity-weighted B−R colour of M31's disk from

Walterbos and Kennicutt (1987) of B−R$\approx$ 1.60 and the colour-M/L relations of Bell and de Jong (2001). These relations yield a mass-to-light ratio of $M/L_R \approx 3.5$. It is important to note that the above B−R colour is uncorrected for reddening due to dust while the Bell and de Jong (2001) relations are for dust-free quantities. However, it is noted by the authors that the dust responsible for the reddening also has the effect of extinguishing the light of the galaxy which increases the mass-to-light ratio. To first order though, these two effects cancel each other out. More careful analysis suggests that the M/L ratio derived using uncorrected colours can be an overestimate by as much as ~ 0.1 dex. Therefore we adopt a value of $M/L_R \approx 3.3$ (uncorrected) for the disk of M31, keeping in mind however, that this ratio could be as low as 2.8.

We can also make an estimate of the corrected or true mass-to-light ratio for the M31 disk. From the work of Burstein and Heiles (1984) we know that the constant foreground reddening inside that Milky Way in the direction of M31 is E(B−V)=0.08 whereas the internal reddening of the disk of M31 is estimated to be E(B−V)$\approx$ 0.25 (Williams and Hodge, 2001) for a total reddening of E(B−V)$\approx$ 0.33. In addition, Barmby et al. (2000) find that for the M31 disk (see their Table 6), E(B−R)$\approx$ 1.6×E(B−V)$\approx$ 0.53. If we correct the B−R colour of the M31 disk by this amount and then use the relations of Bell and de Jong (2001) we find $M/L_R \approx 1.3$. If we compare this to the uncorrected $M/L_R \approx 3.3$ it implies that the extinction in the R-band is ~ 1.0. This number is in good agreement with the estimate of Kent (1989) of ~ 0.99 mag for the total extinction. The agreement of these two quantities gives us confidence in our adopted value for the uncorrected mass-to-light ratio of the M31 disk.

The relationship between the disk mass-to-light ratio and central surface density in our models is $(M/L_R) = 8.4\Sigma_{0,9}$, where $\Sigma_{0,9}$ is Σ_0 in units of 10^9 $M_\odot$ kpc^{-2}, and in Figure 4.2, we show the vertical line in the Σ_0-r_H plane corresponding to $M/L_R = 3.3$. We assert suitable M31 mass models lie on the segment of this line that falls within the existing 99% confidence region. Table 4.2 summarizes the parameters for the

best-fit mass models subject to the additional constraint that $(M/L_R)_D = 3.3$. We will refer to this set of results as the "constrained best-fit" solutions.

In comparing the constrained solutions to the unconstrained results we find that the bulge properties, such as the model mass as well as the realization of the bulge velocity dispersion and surface brightness profiles for the two sets, are nearly identical. Since the mass-to-light constraint forces the disk central surface density down, the disks in the flattened and spherical constrained cases are less massive. The resulting reduction in the disk contribution to the rotation curve is offset by the halo becoming both denser and more concentrated. The overall effect is that the total rotation curves for the constrained and unconstrained cases are nearly the same but the relative contributions of the disk to the overall profile are significantly different. Figure 4.3 illustrates these differences where the solid curves in the two panels show the rotation curves for models subject to the $(M/L_R)_D = 3.3$ constraint; the results for the flattened disk are shown in the upper panel while those for the spherical disk are plotted in the lower panel. Juxtaposed in the plot for comparison are the corresponding results for the unconstrained case as dashed curves. It is obvious from the plot that the halo contribution to the potential is greater than that of the disk at *all* radii for the constrained case. According to Widrow et al. (2003) this property is likely to delay or even suppress the onset of bar formation. Figure 4.4 shows the mass profiles for the constrained (thick lines) and the unconstrained (thin lines) cases, for $r > 10$ kpc. At smaller radii, the constrained and unconstrained results are almost identical. The mass profiles for the two spherical disk models (dotted lines) remain nearly identical all the way out to the virial radius. The constrained flat disk model, however, is more massive than the unconstrained case by about 10% at the virial radius. Finally, we confirm that the normalized fraction of "galactic" baryons for the constrained models are more reasonable in that they are < 1.

4.3 Comparing to Other Mass Models

The work of Kent (1989) was one of the first attempts to construct a detailed mass model of M31 using both photometric and kinematic data. Comparing our constrained best-fit model (Table 4.2) to his small bulge model, we find that the properties of his bulge are broadly comparable to ours though in detail, Kent's bulge is a factor of 1.5 more massive than ours and the corresponding mass-to-light ratio is $(M/L_R)_B = (4.4 \pm 0.4)$[1], compared to our value of 3.3. Kent's disk is approximately twice as massive as ours and the corresponding mass-to-light ratio of (9.0 ± 0.9)[1] is also larger than our value of 3.3. Given the different assumptions underlying our two approaches and the strong coupling between the bulge-disk-halo components, we feel encouraged by the fact that our two results are comparable to within a factor of ~ 2. Among the differences in our two approaches are: (a) Kent (1989) fixed the central surface brightness of his disks to values lower than what we find; (b) he adopted a constant density dark matter halo whereas we assume an NFW functional form; and (c) he modelled the bulge as an oblate spheroid whereas our bulge is spherically symmetric. The precise cause of the differences between our two results is difficult to track down, however, we believe that they are primarily due to assumption (b). As indicated by his Figure 2, the disk is the primary contributor to the rotation curve over the range 5 kpc$< r <$25 kpc whereas in our model the disk does not dominate at any radius.

The work done by Widrow et al. (2003) in developing their M31 model was similar to our approach in that they sought out best-fit solutions by minimizing a composite χ^2 statistic. In fact several of the datasets we use in this work are taken from their paper. However, their approach differs from ours in that they modelled the bulge, disk, and halo components of the galaxy as distribution functions, which cannot be specified analytically. To represent their halo they used a lowered Evans

[1]These values are slightly different from those quoted in Kent (1989) because they have been rescaled to account for the differences in our assumed distance to M31.

model (Kuijken and Dubinski, 1994; Evans, 1993) instead of an NFW-like profile, they represented their bulge by a lowered isothermal sphere or a King model (King, 1966; Binney and Tremaine, 1987), and their disk by a Kuijken and Dubinski (1994) model. This representation of the disk is similar to ours in that the surface density falls off exponentially with radius; unlike us, they also take into account the finite thickness of the disk. Widrow et al. list the properties of their best-fit model as well as a number of variants on that model. In terms of the model's characteristics for $r < 30$ kpc, our constrained best-fit axisymmetric model is similar to their preferred model (Model A), as can be seen by comparing their Figure 4 to Figure 4.3 in this thesis. There are, however, some quantitative differences. Their decomposition of the surface brightness into bulge and disk components gives a bulge-to-disk light ratio of 0.58 versus our ratio of 0.38. This may stem from their use of different functional forms for the bulge and disk, or it may be because they use only the global surface brightness profile from Walterbos and Kennicutt (1987), which does not constrain the bulge region very well. The bulge-to-disk *mass* ratio in contrast, matches ours. As a result their bulge mass-to-light ratio is 2.7, 20% smaller than ours, and their disk mass-to-light ratio is 4.4, 30% larger than ours. The contrast between their bulge and disk M/L ratios is not very reasonable, given that the observed disk colour is slightly bluer than that of the bulge, unless there is substantial dark matter in the disk. After their initial analysis, Widrow et al. replace their lowered Evans model with an NFW halo that closely matches the inner structure of their original halo. This NFW halo has $C_{200} = 11.5$, $r_H = 19.5$ kpc, $R_{200} = 224$ kpc, and $M_{200} = 1.3 \times 10^{12}$ $M_\odot$. The resulting total mass of M31 is a factor of 1.6 greater than that of our system, and is somewhat on the high side in light of the mass constraints displayed in our Figure 3.9. Despite these differences, the disk and halo properties still put their model within the allowed region in Figure 4.2, and in general the differences between their model and ours are not very substantial given the large differences between our functional forms.

Klypin et al. (2002) also construct a mass and light model of M31, in order to test

the consistency of large disk galaxies such as the Milky Way and M31 with the cuspy halos of the ΛCDM paradigm. An interesting feature of this model is their inclusion of adiabatic contraction (Blumenthal et al., 1986) of their *initially* NFW halos by the gravity of the disk and the bulge. They use a four component model to represent the baryonic component and halo which contains a flattened bulge, a bar, an exponential disk, and the halo. These four components contain 14 parameters in total. Their paper does not actually state the parameter values or how the parameters were chosen, but they assert that the chosen values achieve a good match to the data without the need for careful optimization. Their treatment of the dynamics of the bulge and disk are even more approximate than ours; the central mass profile is calculated from an isothermal sphere approximation, and the disk rotation curve apparently does not take flattening into account. Given these differences in the approach to our models, some differences from our results are to be expected. Nevertheless, we do find a remarkable level of agreement between their Model C1 and our best-fit constrained model, as can be seen by comparing their Figure 4 to Figure 4.3 in this thesis. One primary difference between these two models is that their bulge-disk decomposition is different, with the mass ratio between the two being only 0.27 whereas in our model it is 0.37. This difference could be a product of the modelling of the dynamics or the different bulge profiles. A second difference is in the total R-band luminosity, if we correct their unextincted luminosity to extincted using the transformations they suggest, they obtain a total galaxy R luminosity of 3.5×10^{10} $L_\odot$ or 16% larger than ours. We do not understand the origin of this difference, since we are using nearly the same data and they have not raised the Walterbos and Kennicutt (1987) surface brightness by 0.1 mag arcsec^{-2} as we have. Together with their total baryonic component mass, which is smaller than ours by 10%, this gives $M/L_R = 2.5$ (extincted) whereas in our model it is 3.3. A third difference is in the halo masses, their halo being slightly more massive than ours. Overall, we estimate that the mass of their total system within 125 kpc is approximately $0.9 - 1.0 \times 10^{12}$ $M_\odot$ whereas our best-fit constrained model

is roughly a factor of 1.4 less massive. This difference is probably within the large errors on the halo mass and is not necessarily a product of our different modelling technique.

In their analysis of the stream dynamics, Ibata et al. (2004) considered three toy potentials as well as a variant of the Klypin et al. (2002) Model C1 in which the bulge and disk properties were kept fixed to the values specified by Klypin et al., but the halo properties were allowed to vary with the aim of minimizing discrepancies between the orbit of the progenitor and that of the giant stream. Depending on which stream constraints they used, Ibata et al. (2004) iterated to two models. The rotational velocity and the total mass profiles (computed from the rotation curve using the spherical approximation) for these two models are shown as dashed and dot-dashed lines in the lower panel of Figure 3.7 and Figure 3.9, respectively. As illustrated in Figure 3.7, the rotation curve for the model dubbed "high mass" by Ibata et al. (2004) is in conflict with the observations. Ibata et al. (2004) note this and reject the model on this basis. The characteristics of the alternate "low mass" model are broadly similar to those of our constrained best-fit axisymmetric case, and for the purposes of orbit calculations, we expect that the two will give broadly similar results. However, the fact that the Ibata et al. (2004) system has 10% more mass within 125 kpc will, for a given set of initial conditions, lead to small differences in the apocentre. This point will be discussed further in the next chapter.

For completeness, we also show in Figures 3.7 and 3.9 the rotation and total mass profiles for two of Ibata et al.'s toy spherically symmetric models, one with an NFW density profile and potential

$$\Phi(r) = -\frac{GM_s}{r}\ln(1 + r/r_s), \tag{4.2}$$

where $r_s = 13.1$ kpc is the scale radius and M_s, the mass within $5.3r_s$, is $M_s = 4.4 \times 10^{11}$ $M_\odot$, and the other with a logarithmic potential

$$\Phi(r) = \frac{1}{2}V_c^2 \ln(r_c^2 + r^2), \tag{4.3}$$

where the core radius r_c is taken to be 3 kpc and $V_c = 162$ km s^{-1}. These two models are plotted as the lower dot-dashed line and short-dashed-long-dashed curves, respectively. Neither of the two models are in agreement with the observed rotation curve data. They also both significantly underestimate the depth of the potential (and the mass) within 100 kpc.

In their recent study, Font et al. (2005) adopted the axisymmetric bulge-disk-halo model of Bekki et al. (2001) with potential

$$\Phi(r) = \Phi_B(r) + \Phi_D(r) + \Phi_H(r), \tag{4.4}$$

where,

$$\Phi_B(r) = -\frac{GM_B}{r_B + r}, \tag{4.5}$$

$$\Phi_D(r) = -\frac{GM_D}{\sqrt{R^2 + (a + \sqrt{z^2 + b^2})^2}}, \tag{4.6}$$

$$\Phi_H(r) = V_H^2 \ln(r_c^2 + r^2), \tag{4.7}$$

r is the distance from the centre of the galaxy, R and z are polar coordinates aligned with the plane of M31's disk, $r_c = 12$ kpc, $V_H = 131.5$ km s^{-1}, $M_D = 1.3 \times 10^{11}$ M$_\odot$, $a = 6.5$ kpc, $b = 0.26$ kpc, $M_B = 9.2 \times 10^{10}$ M$_\odot$, and $r_B = 0.7$ kpc. For comparative purposes, the rotation curve and the total mass profiles (computed from the rotation curve using the spherical approximation) for this model are plotted in Figures 3.7 and 3.9 as dotted curves. It is clear in Figure 3.7 that the model rotation curve is systematically higher than the observed profile, with the two being the least discrepant in the outer disk region where the model curve is approximately 20 km s^{-1} higher,

and most discrepant in the inner regions of the disk. The latter is primarily due to the large bulge mass assumed by Bekki et al. (2001). Their bulge mass is $\sim$ 3 times larger than ours. Additionally the Bekki et al. model overestimates the mass beyond $\sim$ 80 kpc. Overall the galaxy described by this model has a much deeper potential than that indicated by the observations or that described by our preferred M31 model. The next chapter of this thesis will illustrate how this deeper potential has significant implications for orbit calculations.

Finally Merrett et al. (2003) (see also Merrett et al. (2004)), in their efforts to model the dynamics of the recently discovered planetary nebulae in and about the disk of M31, model M31 as a mildly flattened singular isothermal sphere:

$$\Phi(R,z) = \frac{1}{2}V_c^2 \ln\left(R^2 + \frac{z^2}{q^2}\right), \tag{4.8}$$

with $V_c = 250$ km s^{-1} and a value of $q = 0.9$ for the flattening. For the discussion in the next chapter on test particle orbits, we adopt as a foil a slightly modified version of this potential. Specifically, we set the flattening parameter to q=1 and consider the corresponding spherically symmetric isothermal sphere model for M31 with potential:

$$\Phi(r) = V_c^2 \ln(r), \tag{4.9}$$

where $V_c = 250$ km s^{-1} is the circular velocity. The corresponding rotation and total mass profiles of this singular isothermal sphere model are shown in Figures 3.7 and 3.9 as long-dashed lines. This model is the simplest possible model for M31. The circular velocity is tuned to match the observed rotation profile but as is apparent in Figure 3.9, the model greatly overestimates the system mass beyond $\sim$ 80 kpc.

Chapter 5

Sample Orbits in Spherical and Flattened Disk Potentials

With our mass models defined, we are now in a position to study the orbits that give rise to the giant southern stream in M31. The main focus in this thesis is to study some of the effects seen when using our mass models, versus some other models that have been previously used for this purpose. The results of our detailed study of the stream orbits are not the main focus of this thesis and the reader is referred to Fardal et al. (2005) for details of the study.

5.1 Summary of Observation of the Stream

Though it has only been discovered recently, the amount of observational data available about the giant southern stream already approaches that which is available for the Sagittarius stream in our own galaxy. Before going further with the discussion of the sample orbits we pause to discuss what is currently known about the southern stream.

The stream itself extends to the SE of the galaxy for approximately 5° on the

Table 5.1 Kinematic data for the southern stream, in units where M31 is at the centre. A dash indicates that there is no data for that field. The angular positions ξ and η are those of the field centres; field "a3" is certainly offset from the position of the stream, while fields 1-8 may be as well. Data for satellite galaxies of M31 is found at the bottom of the table.

Field/Name	ξ (deg)	η (deg)	d' (kpc)	v'_r (km s^{-1})
a3	+1.077	−2.021	66	−158
1	+2.015	−3.965	102	0
2	+1.745	−3.525	93	−50
3	+1.483	−3.087	76	—
4	+1.226	−2.653	71	—
5	+0.969	−2.264	56	—
6	+0.717	−1.768	52	−180
7	+0.467	−1.327	45	—
8	+0.219	−0.886	−4	−300
12	−0.731	+0.891	−45	—
13	−0.963	+1.342	−26	—
M32	+0.0	−0.4	0	+100
NGC 205	−0.5	+0.4	50	+55
And VIII	+0.1	−0.7	—	−205

sky. The stream visibly peters out near Field 1 of McConnachie et al. (2003) as seen in the larger survey presented in Ferguson et al. (2004), however the total extent of the stream is not well known. The northern part of the stream is eventually lost to confusion against the disk of M31. An estimate of the stellar mass in the stream can be found if we assume a mass-to-light ratio of $M/L_V \approx 7$ and a stream luminosity of $\sim 3.4 \times 10^7$ $L_\odot$, which gives an estimate of $\sim 2.4 \times 10^8$ $M_\odot$. The work of Guhathakurta et al. (2005) determined a mean metallicity for the stream of [Fe/H]≈ -0.5 which suggests that the progenitor had a much larger total luminosity of $\sim 10^9$ $L_\odot$ (Font et al., 2005). McConnachie et al. (2003) suggest that the stream continues at least 1.5° to the NW on the near side of M31, however this is questionable for several reasons: this extension is not a distinct surface brightness feature (Ferguson et al., 2004), as yet there is no spectroscopic confirmation of a stream component, and as shown by Ibata et al. (2004) this extension is difficult to derive an orbit for. Later in this chapter we will show that we also find it difficult to fit this feature.

Field positions, distances, and velocities for published observations of the stream are found in Table 5.1, along with data on M31 and some of its satellite galaxies (M32, NGC 205, and And VII). The positional data show that the stream is a roughly linear structure, at least in projection. Note that the field "a3" of Guhathakurta et al. (2005) overlaps the stream only by chance, and is not centred on the stream. Although fields 1-8 of McConnachie et al. (2003) follow the path of the stream on the sky, they only approximately lie along the centre of the stream. Some of these positions were chosen by extrapolating from the inner part of the stream. Their Figure 3 shows a histogram of stars as a function of transverse position which suggests that the central ridge of the stream is offset fairly uniformly by $\sim 0.15°$ from the field centres. There is a further concern about Field 8 due to its proximity to the disk of M31; its stars may suffer from contamination from the disk.

5.2 Constructing the Sample Orbits

We start our orbit calculations by adopting the initial conditions of Font et al. (2005) to facilitate comparisons between our work and theirs. The orbits presented by these authors are in rough agreement with kinematic observations of the giant southern stream made by McConnachie et al. (2003), Law et al. (2004), Ibata et al. (2004), and Guhathakurta et al. (2005), however, they were constructed under the assumption that both the stream and the progenitor follow the same orbit. This is the simplest assumption to make in such initial analyses, and we make the same assumption in this work, however in reality the stream exists precisely because the stream stars are on slightly *different* orbits than the progenitor (Fardal et al., 2005). The work of Fardal et al. (2005) builds on this assumption and makes an approximation which takes into account the difference between the stream and the orbit of the progenitor. The orbits presented in this thesis are computed in a rectangular right-handed coordinate system (x, y, z) which is centred on M31 and oriented to the sky such that x points east, y points north and z points away from us, parallel to the line of sight. The observed quantities, however, are not obtained in a rectangular coordinate system because M31 is so close the system has a significant width and depth on the sky. Since there is insufficient information to correct all the observations to rectangular coordinates, we therefore convert the orbits to observed coordinates instead. The positional coordinates, ξ and η are standard coordinates on the tangent plane. The following formulae provide the east-west coordinate η, the north-south coordinate ξ, the distance d, and the radial velocity v_r:

$$\xi = x/(z_g + z), \tag{5.1}$$

$$\eta = y/(z_g + z), \tag{5.2}$$

$$d = [x^2 + y^2 + (z_g + z)^2)]^{1/2} \equiv d' + z_g, \tag{5.3}$$

$$v_r = d^{-1}[x(v_x + v_{gx}) + y(v_y + v_{gy}) + (z_g + z)(v_z + v_{gz})] \equiv v_r' + v_{gz}, \tag{5.4}$$

where $z_g = 784 \pm 24$ kpc and $v_{gz} = -300 \pm 4$ km s^{-1} are the distance and mean radial velocity of M31 as quoted before from Stanek and Garnavich (1998) and de Vaucouleurs et al. (1991), respectively. In the plots presented in this chapter we use the relative distance d' (which we refer to as the "depth") and the relative velocity v_r', found by subtracting the mean distance and radial velocity of M31.

The test particle orbits were calculated by solving Newton's equation of motion, $\vec{F} = m\vec{a}$. The force on a particle is related to the potential of the galaxy by $\vec{F} = -m\nabla\Phi$. The following equation must now be solved

$$\frac{d^2\vec{r}}{dt^2} = -\nabla\Phi(r), \tag{5.5}$$

where $\vec{r} = (x, y, z)$ and $\Phi(r)$ is the potential of M31 as defined previously. The velocity of the particle is related to its position through

$$\frac{d\vec{r}}{dt} = \vec{v}. \tag{5.6}$$

Equations 5.5 and 5.6 have three components each, x, y, and z which means we must solve six differential equations to calculate the orbit of the test particle.

These equations were solved using a fourth-order Runge-Kutta ODE integrator routine with an adaptive stepsize control. The Runge-Kutta method of integrating ODEs takes a series of "trial" steps (depending on the order, our routine takes three steps) across an interval and then computes the "real" step over the whole interval. The method expressed mathematically is

$$k_1 = hf(x_n, y_n), \tag{5.7}$$

$$k_2 = hf(x_n + \frac{h}{2}, y_n + \frac{k_1}{2}), \tag{5.8}$$

$$k_3 = hf(x_n + \frac{h}{2}, , y_n + \frac{k_2}{2}), \tag{5.9}$$

$$k_4 = hf(x_n + \frac{h}{2}, , y_n + \frac{k_3}{2}), \tag{5.10}$$

$$y_{n+1} = y_n + \frac{k_1}{6} + \frac{k_2}{3} + \frac{k_3}{3} + \frac{k_4}{6} + O(h^5). \tag{5.11}$$

Here $dy/dx = f(x, y)$ and h is the step size. The fourth-order Runge-Kutta method makes four evaluations of the derivative, once at the initial point (k_1), twice at trial midpoints (k_2 and k_3), and once at a trial endpoint (k_4). The advantage of using an adaptive stepsize routine is that small steps can used through regions where care must be taken due to the behaviour of the function in that regions and larger stepsizes can be used in regions where the behaviour of the function is smoother (Press et al., 1992).

To start this exercise of constructing test particle orbits, we gently adjust the Font et. al. initial conditions to match the observations of the stream, using our toy spherical disk potential. Note that no attempt has been made to use statistics to optimize our results. The purpose of the orbits presented in this chapter is to demonstrate the effect that the potential has on the orbits. The primary "constraint" we have used is that the apocentre of the orbit must occur approximately at Field 1, since the radial velocity of the stream relative to M31 is nearly zero there.

We compare the test particle orbits corresponding to our new initial conditions computed in two different potentials in Figure 5.1. The solid curve shows our best fit spherically symmetric mass model while the dashed curve shows the simple singular isothermal sphere halo. Since both potentials are spherically symmetric, the shape of the mass distribution is not an issue and it should not be surprising that the overall

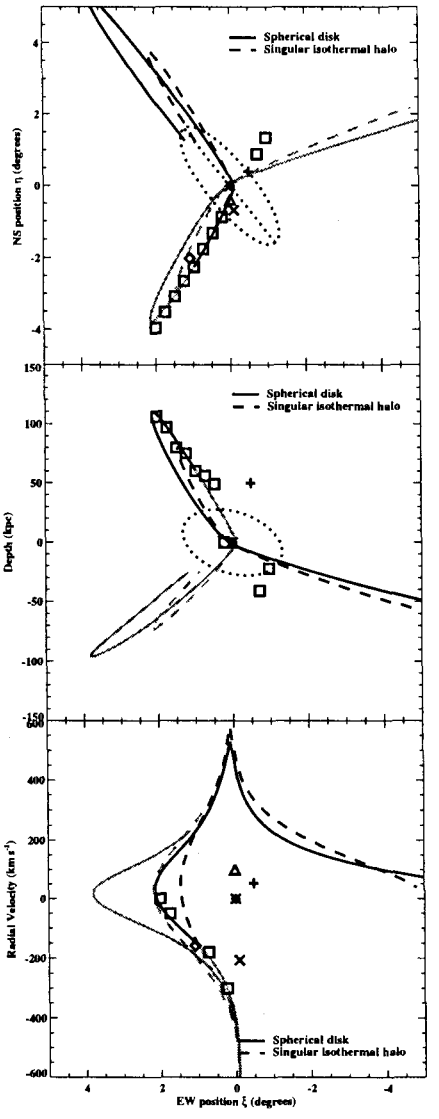

Figure 5.1 Compares the orbits resulting from a singular isothermal sphere potential and our spherical disk potential. The solid curve shows our spherical potential with the initial velocities set so that the orbit turns around at Field 1. The dashed line shows the orbit of the singular isothermal sphere potential potential with the same initial conditions as the spherical disk. Grey and black curves represent orbit integrations forward and backward in time, respectively. *(Top panel):* shows how the orbit looks in sky coordinates, ξ and η. *(Middle panel):* plots the line-of-sight depth (in kpc) of the orbit versus the ξ position in the sky. *(Bottom panel):* plots the variation of radial velocity (in km s^{-1}) with ξ position in the sky. The symbols in the three panels are as follows: star (M31), open triangle (M32), plus (NGC 205), open diamond (Field a3), cross (And VIII), open squares (stream fields).

shapes of the orbits are very similar. Therefore, any differences between the two orbits are due to the difference in the radial mass distribution (see Figure 3.9). It is clear from the mass distribution plot that the singular isothermal potential is a much deeper potential and consequently, when tracing the orbit backwards in time, the test particle is unable to climb out as far before reaching apocentre and falls short of Field 1 by approximately one degree. Figure 3.9 shows that the Bekki et al. (2001) model used by Font et al. (2005) is also deeper than our spherical and flattened disk models, however, not as deep as the singular isothermal potential and we therefore expect a similar though smaller difference if we compared our orbits to those resulting from their model. Put another way, Font et. al. require higher initial velocities to guarantee that their orbit's apocentre are coincident with Field 1.

The next step in our study of these orbits is to test the effect that the geometry of the mass distribution has on the orbits. Figure 5.2 compares the difference between orbits using our best-fit flattened disk model and our best-fit spherical disk model, using the same initial conditions as before. Note that these initial conditions were chosen to ensure that the apocentre of the test particle in our best-fit *spherical* disk model coincides with Field 1. This figure shows that these two cases are more similar than the pair shown in the previous figure, however there are still some significant observational differences.

To understand the source of the differences between the two orbits it is useful to employ an intermediate step. The dotted curve in the plot shows the results using the *flattened disk model parameters* with the *spherical disk formula for the potential* (Equation 2.6). These results nearly overlap those from the flattened disk model over the duration of the lobe which includes the stream. However, the directions of the preceding and subsequent lobes are quite different. The reason for this is that these parts of the particle's trajectory are very sensitive to the differences in the geometry of the disk potential at pericentre, since at this point the test particle plunges all the way in to where the disk contribution to the total potential is significant. The

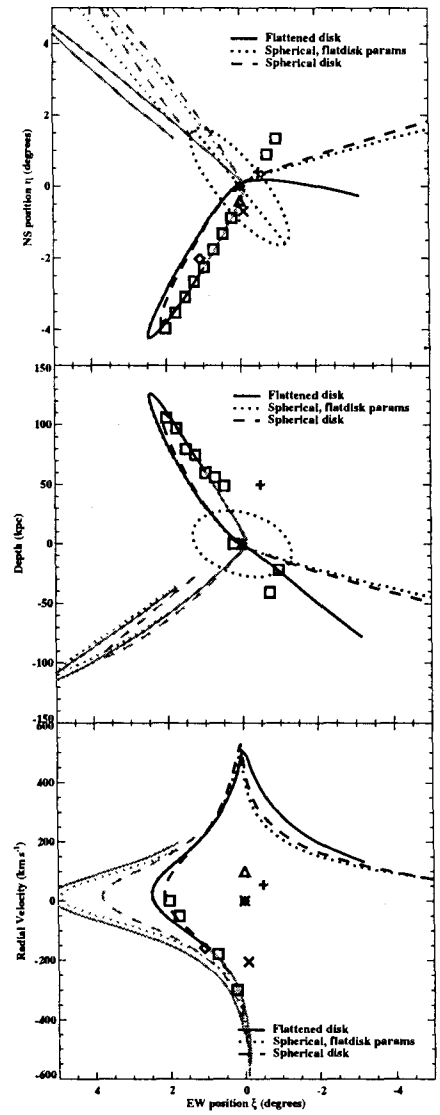

Figure 5.2 The above three panels show a comparison between the orbits resulting from our axisymmetric and spherical potentials, and our spherical potential with its parameters replaced by those of the axisymmetric potential. All panels, symbols, and colours are the same as in Figure 5.1, however, the solid line now represents our axisymmetric potential, the dotted line our spherical potential with the parameters of the axisymmetric potential, and the dashed line represents the spherical disk. All orbits are calculated using the same initial conditions as in Figure 5.1. This is why only the spherical potential orbit turns around at Field 1 while the other two orbits overshoot this field. Note also that the time intervals for the different orbits are not the same.

gravitational pull from the disk pulls the test particle towards the plane of the disk, resulting in an orbit that bends more strongly than in the spherical case.

The second step is to change the parameters to those of the best-fit spherical model. As discussed earlier the differences between the parameters for the two models are minor. Still, they make a visible difference *within* the radial lobes. Figure 3.9 illustrates that the flattened disk potential is shallower than the spherical model, so the apocentre of the stream is still larger, and the gradient of the velocity with position is smaller. For the flattened disk orbit to coincide with Field 1 we would clearly need to change the initial conditions somewhat. Evidently, even small changes in the mass profile between these two models can potentially be detected using the stream as a dynamical tracer.

In summary, the radial mass profile has a significant effect on orbits in the halo, and is the primary factor in determining the length of the stream given the initial velocity, or alternatively the gradient of the velocity given the length of the stream. The geometric shape of the mass profile is a less significant factor, at least with the tests that have been performed in this work, but it does play a significant role in determining the direction of subsequent lobes. If part of the objective for computing the orbits is to try to ascertain where the stream progenitor may be, then it is important to compute the orbits in a realistically shaped potential. An interesting direction to explore in the future is to test the effect that the flattening of the halo has on the computation of orbits.

Chapter 6

Summary

This work has taken a step forward in that we have improved upon on previous attempts to model the Andromeda galaxy. There are several significant results from this work that are important to highlight. Probably the most important result from this work is that we have presented a simple analytic model for the mass density, light density, and gravitational potential of M31, which is easy to use for the purposes of orbit calculations. As this is the first step in a larger study, this potential is applied to the problem of estimating the orbit and other properties of the giant southern stream in M31's halo in Fardal et al. (2005). The potential presented here does a better job matching the dynamics of M31 than other simple potentials used recently to model the dynamics of the stream. It does a comparable job, and in fact is fairly similar in its properties, to several more sophisticated but non-analytic models found in the literature. The eight parameters which describe this mass and light model span a large but low-dimensional region in parameter space. Using various physical constraints on the fraction of baryons in the galaxy, the halo concentration, the mass within 125 kpc, and the stellar mass-to-light ratio we restrict the parameters to a much smaller region. While our formal best-fit is ruled out by these constraints, we can still construct a model that is physically acceptable and fits the observations well.

The parameters of this model and its important physical quantities are summarized in Table 4.2.

In constructing our sample test particle orbits we were able to make conclusions about the effect of the geometry and radial mass profile of the galaxy. We found that the radial mass profile has a significant effect on orbits within the giant southern stream, and is the determining factor in the length of the stream for a given initial velocity. A simple and fairly accurate way to evaluate orbits in M31's halo is to use the parameters in our model but assume a spherically symmetric mass profile, ignoring the flattening of the disk. The effect of the geometric shape of the mass profile is not as significant as the radial mass profile itself. However, it does have an effect on the direction of subsequent lobes of the orbit. This becomes important if one wishes to construct orbits for the purposes of locating the progenitor of the stream.

Bibliography

Babcock, H. W.: 1938, *PASP* **50**, 174

Babcock, H. W.: 1939, *Lick Observatory Bulletin* **19**, 41

Bacon, R., Emsellem, E., Combes, F., Copin, Y., Monnet, G., and Martin, P.: 2001, *A&A* **371**, 409

Barmby, P., Huchra, J. P., Brodie, J. P., Forbes, D. A., Schroder, L. L., and Grillmair, C. J.: 2000, *AJ* **119**, 727

Bekki, K., Couch, W. J., Drinkwater, M. J., and Gregg, M. D.: 2001, *ApJ* **557**, L39

Bell, E. F. and de Jong, R. S.: 2001, *ApJ* **550**, 212

Binney, J. and Tremaine, S.: 1987, *Galactic dynamics*, Princeton, NJ, Princeton University Press, 1987, 747 p.

Blumenthal, G. R., Faber, S. M., Flores, R., and Primack, J. R.: 1986, *ApJ* **301**, 27

Braun, R.: 1991, *ApJ* **372**, 54

Bullock, J. S., Kolatt, T. S., Sigad, Y., Somerville, R. S., Kravtsov, A. V., Klypin, A. A., Primack, J. R., and Dekel, A.: 2001, *MNRAS* **321**, 559

Burstein, D. and Heiles, C.: 1984, *ApJS* **54**, 33

Côté, P., Mateo, M., Olszewski, E. W., and Cook, K. H.: 1999, *ApJ* **526**, 147

de Vaucouleurs, G.: 1948, *Annales d'Astrophysique* **11**, 247

de Vaucouleurs, G., de Vaucouleurs, A., Corwin, H. G., Buta, R. J., Paturel, G., and Fouque, P.: 1991, *Third Reference Catalogue of Bright Galaxies*, Volume 1-3, XII, 2069 pp. 7 figs.. Springer-Verlag Berlin Heidelberg New York

Deharveng, J. M. and Pellet, A.: 1975, *A&A* **38**, 15

Dehnen, W.: 1993, *MNRAS* **265**, 250

Dolag, K., Bartelmann, M., Perrotta, F., Baccigalupi, C., Moscardini, L., Meneghetti, M., and Tormen, G.: 2004, *A&A* **416**, 853

Dressler, A. and Richstone, D. O.: 1988, *ApJ* **324**, 701

Dutton, A. A., Courteau, S., de Jong, R., and Carignan, C.: 2003, *ArXiv Astrophysics e-prints*

Evans, N. W.: 1993, *MNRAS* **260**, 191

Evans, N. W. and Wilkinson, M. I.: 2000, *MNRAS* **316**, 929

Evans, N. W., Wilkinson, M. I., Guhathakurta, P., Grebel, E. K., and Vogt, S. S.: 2000, *ApJ* **540**, L9

Fardal, M. A., Babul, A., Geehan, J. J., and Guhathakurta, P.: 2005, *ArXiv Astrophysics e-prints*

Ferguson, A., Chapman, S., Ibata, R., Irwin, M., Lewis, G., and McConnachie, A.: 2004, *ArXiv Astrophysics e-prints*

Ferguson, A. M. N., Irwin, M. J., Ibata, R. A., Lewis, G. F., and Tanvir, N. R.: 2002, *AJ* **124**, 1452

Ferguson, A. M. N., Johnson, R. A., Faria, D. C., Irwin, M. J., Ibata, R. A., Johnston, K. V., Lewis, G. F., and Tanvir, N. R.: 2005, *ApJ* **622**, L109

Fioc, M. and Rocca-Volmerange, B.: 1997, *A&A* **326**, 950

Font, A., Johnston, K. V., Guhathakurta, P., Majewski, S. R., and Rich, R. M.: 2005, *ArXiv Astrophysics e-prints*

Guhathakurta, P., Reitzel, D. B., and Grebel, E. K.: 2000, in *Proc. SPIE Vol. 4005, p. 168-179, Discoveries and Research Prospects from 8- to 10-Meter-Class Telescopes, Jacqueline Bergeron; Ed.*, pp 168–179

Guhathakurta, P., Rich, R. M., Reitzel, D. B., Cooper, M. C., Gilbert, K. M., Majewski, S. R., Ostheimer, J. C., Geha, M. C., Johnston, K. V., and Patterson, R. J.: 2005, *ArXiv Astrophysics e-prints*

Helmi, A. and White, S. D. M.: 1999, *MNRAS* **307**, 495

Hernquist, L.: 1990, *ApJ* **356**, 359

Hoessel, J. G. and Melnick, J.: 1980, *A&A* **84**, 317

Ibata, R., Chapman, S., Ferguson, A. M. N., Irwin, M., Lewis, G., and McConnachie, A.: 2004, *MNRAS* **351**, 117

Ibata, R., Irwin, M., Lewis, G., Ferguson, A. M. N., and Tanvir, N.: 2001a, *Nature* **412**, 49

Ibata, R., Irwin, M., Lewis, G. F., and Stolte, A.: 2001b, *ApJ* **547**, L133

Ibata, R., Lewis, G. F., Irwin, M., Totten, E., and Quinn, T.: 2001c, *ApJ* **551**, 294

Ibata, R. A., Gilmore, G., and Irwin, M. J.: 1995, *MNRAS* **277**, 781

Ibata, R. A., Irwin, M. J., Lewis, G. F., Ferguson, A. M. N., and Tanvir, N.: 2003, *MNRAS* **340**, L21

Innanen, K. A., Kamper, K. W., van den Bergh, S., and Papp, K. A.: 1982, *ApJ* **254**, 515

Johnston, K. V., Hernquist, L., and Bolte, M.: 1996, *ApJ* **465**, 278

Jorgensen, I.: 1994, *PASP* **106**, 967

Kent, S. M.: 1983, *ApJ* **266**, 562

Kent, S. M.: 1987, *AJ* **94**, 306

Kent, S. M.: 1989, *PASP* **101**, 489

King, I. R.: 1966, *AJ* **71**, 64

Klypin, A., Zhao, H., and Somerville, R. S.: 2002, *ApJ* **573**, 597

Kormendy, J.: 1988, *ApJ* **325**, 128

Kormendy, J. and Bender, R.: 1999, *ApJ* **522**, 772

Kormendy, J. and Richstone, D.: 1995, *ARA&A* **33**, 581

Kuijken, K. and Dubinski, J.: 1994, *MNRAS* **269**, 13

Lauer, T. R., Faber, S. M., Groth, E. J., Shaya, E. J., Campbell, B., Code, A., Currie, D. G., Baum, W. A., Ewald, S. P., Hester, J. J., Holtzman, J. A., Kristian, J., Light, R. M., Ligynds, C. R., O'Neil, E. J., and Westphal, J. A.: 1993, *AJ* **106**, 1436

Law, D. R., Johnston, K. V., and Majewski, S. R.: 2004, *ArXiv Astrophysics e-prints*

Lee, M. G., Freedman, W. L., and Madore, B. F.: 1993, *ApJ* **417**, 553

Lindblad, B.: 1956, *Stockholms Observatoriums Annaler* 2

Ma, J., Peng, Q., and Gu, Q.: 1997, *ApJ* **490**, L51+

Majewski, S. R., Siegel, M. H., Kunkel, W. E., Reid, I. N., Johnston, K. V., Thompson, I. B., Landolt, A. U., and Palma, C.: 1999, *AJ* **118**, 1709

Mateo, M., Olszewski, E. W., and Morrison, H. L.: 1998, *ApJ* **508**, L55

McConnachie, A. W., Irwin, M. J., Ibata, R. A., Ferguson, A. M. N., Lewis, G. F., and Tanvir, N.: 2003, *MNRAS* **343**, 1335

McElroy, D. B.: 1983, *ApJ* **270**, 485

Merrett, H., Merrifield, M., Kuijken, K., Romanowsky, A., Douglas, N., Napolitano, N., Arnaboldi, M., Capaccioli, M., Freeman, K., Gerhard, O., Carter, D., Evans, N. W., Wilkinson, M., Halliday, C., and Bridges, T.: 2004, *ArXiv Astrophysics e-prints*

Merrett, H. R., Kuijken, K., Merrifield, M. R., Romanowsky, A. J., Douglas, N. G., Napolitano, N. R., Arnaboldi, M., Capaccioli, M., Freeman, K. C., Gerhard, O., Evans, N. W., Wilkinson, M. I., Halliday, C., Bridges, T. J., and Carter, D.: 2003, *MNRAS* **346**, L62

Mo, H. J. and Mao, S.: 2004, *MNRAS* **353**, 829

Monnet, G. and Simien, F.: 1977, *A&A* **56**, 173

Morris, P. W., Reid, I. N., Griffiths, W. K., and Penny, A. J.: 1994, *MNRAS* **271**, 852

Morrison, H. L., Harding, P., Hurley-Keller, D., and Jacoby, G.: 2003, *ApJ* **596**, L183

Navarro, J. F., Frenk, C. S., and White, S. D. M.: 1996, *ApJ* **462**, 563

Newberg, H. J., Yanny, B., Rockosi, C., Grebel, E. K., Rix, H., Brinkmann, J., Csabai, I., Hennessy, G., Hindsley, R. B., Ibata, R., Ivezić, Z., Lamb, D., Nash, E. T., Odenkirchen, M., Rave, H. A., Schneider, D. P., Smith, J. A., Stolte, A., and York, D. G.: 2002, *ApJ* **569**, 245

Peng, C. Y.: 2002, *AJ* **124**, 294

Press, W. H., Teukolsky, S. A., Vetterling, W. T., and Flannery, B. P.: 1992, *Numerical recipes in FORTRAN. The art of scientific computing*, Cambridge: University Press, —c1992, 2nd ed.

Pritchet, C.: 1977, *ApJS* **35**, 397

Rubin, V. C. and D'Odorico, S.: 1969, *A&A* **2**, 484

Salow, R. M. and Statler, T. S.: 2004, *ApJ* **611**, 245

Sawa, T. and Sofue, Y.: 1982, *PASJ* **34**, 189

Schmidt, M.: 1957, *Bull. Astron. Inst. Netherlands* **14**, 17

Schwarzschild, M.: 1954, *AJ* **59**, 273

Simien, F., Pellet, A., and Monnet, G.: 1979, *A&A* **72**, 12

Spergel, D. N., Verde, L., Peiris, H. V., Komatsu, E., Nolta, M. R., Bennett, C. L., Halpern, M., Hinshaw, G., Jarosik, N., Kogut, A., Limon, M., Meyer, S. S., Page, L., Tucker, G. S., Weiland, J. L., Wollack, E., and Wright, E. L.: 2003, *ApJS* **148**, 175

Stanek, K. Z. and Garnavich, P. M.: 1998, *ApJ* **503**, L131+

Stark, A. A.: 1977, *ApJ* **213**, 368

Stark, A. A. and Binney, J.: 1994, *ApJ* **426**, L31

Tenjes, P., Haud, U., and Einasto, J.: 1994, *A&A* **286**, 753

Totten, E. J. and Irwin, M. J.: 1998, *MNRAS* **294**, 1

Tremaine, S., Gebhardt, K., Bender, R., Bower, G., Dressler, A., Faber, S. M., Filippenko, A. V., Green, R., Grillmair, C., Ho, L. C., Kormendy, J., Lauer, T. R., Magorrian, J., Pinkney, J., and Richstone, D.: 2002, *ApJ* **574**, 740

Walterbos, R. A. M. and Kennicutt, R. C.: 1987, *A&AS* **69**, 311

Walterbos, R. A. M. and Kennicutt, R. C.: 1988, *A&A* **198**, 61

Wechsler, R. H., Bullock, J. S., Primack, J. R., Kravtsov, A. V., and Dekel, A.: 2002, *ApJ* **568**, 52

Weinberg, M. D. and Katz, N.: 2002, *ApJ* **580**, 627

Widrow, L. M., Perrett, K. M., and Suyu, S. H.: 2003, *ApJ* **588**, 311

Williams, B. F. and Hodge, P. W.: 2001, *ApJ* **548**, 190

Wyse, A. B. and Mayall, N. U.: 1942, *ApJ* **95**, 24

Yanny, B., Newberg, H. J., Grebel, E. K., Kent, S., Odenkirchen, M., Rockosi, C. M., Schlegel, D., Subbarao, M., Brinkmann, J., Fukugita, M., Ivezić, Ž., Lamb, D. Q., Schneider, D. P., and York, D. G.: 2003, *ApJ* **588**, 824

Yanny, B., Newberg, H. J., Kent, S., Laurent-Muehleisen, S. A., Pier, J. R., Richards, G. T., Stoughton, C., Anderson, J. E., Annis, J., Brinkmann, J., Chen, B., Csabai, I., Doi, M., Fukugita, M., Hennessy, G. S., Ivezić, Ž., Knapp, G. R., Lupton, R., Munn, J. A., Nash, T., Rockosi, C. M., Schneider, D. P., Smith, J. A., and York, D. G.: 2000, *ApJ* **540**, 825

Zucker, D. B., Kniazev, A. Y., Bell, E. F., Martínez-Delgado, D., Grebel, E. K., Rix, H., Rockosi, C. M., Holtzman, J. A., Walterbos, R. A. M., Annis, J., York, D. G., Ivezić, Ž., Brinkmann, J., Brewington, H., Harvanek, M., Hennessy, G., Kleinman, S. J., Krzesinski, J., Long, D., Newman, P. R., Nitta, A., and Snedden, S. A.: 2004, *ApJ* **612**, L121